NAVAL POSTGRADUATE SCHOOL

MONTEREY, CALIFORNIA

THESIS

MINIATURIZED NEUTRON RADIATION DETECTOR USING BORON-NITRIDE AND MULTI-WALLED CARBON NANOTUBES

by

Kyle M. Surovec

June 2023

Thesis Advisor: Dragoslav Grbovic
Co-Advisor: Craig F. Smith

THIS PAGE INTENTIONALLY LEFT BLANK

REPORT DOCUMENTATION PAGE	*Form Approved OMB No. 0704-0188*

Public reporting burden for this collection of information is estimated to average 1 hour per response, including the time for reviewing instruction, searching existing data sources, gathering and maintaining the data needed, and completing and reviewing the collection of information. Send comments regarding this burden estimate or any other aspect of this collection of information, including suggestions for reducing this burden, to Washington headquarters Services, Directorate for Information Operations and Reports, 1215 Jefferson Davis Highway, Suite 1204, Arlington, VA 22202-4302, and to the Office of Management and Budget, Paperwork Reduction Project (0704-0188) Washington, DC, 20503.

1. AGENCY USE ONLY *(Leave blank)*	**2. REPORT DATE** June 2023	**3. REPORT TYPE AND DATES COVERED** Master's thesis

4. TITLE AND SUBTITLE MINIATURIZED NEUTRON RADIATION DETECTOR USING BORON-NITRIDE AND MULTI-WALLED CARBON NANOTUBES	**5. FUNDING NUMBERS** RPL34
6. AUTHOR(S) Kyle M. Surovec	
7. PERFORMING ORGANIZATION NAME(S) AND ADDRESS(ES) Naval Postgraduate School Monterey, CA 93943-5000	**8. PERFORMING ORGANIZATION REPORT NUMBER**
9. SPONSORING / MONITORING AGENCY NAME(S) AND ADDRESS(ES) Defense Threat Reduction Agency	**10. SPONSORING / MONITORING AGENCY REPORT NUMBER**

11. SUPPLEMENTARY NOTES The views expressed in this thesis are those of the author and do not reflect the official policy or position of the Department of Defense or the U.S. Government.

12a. DISTRIBUTION / AVAILABILITY STATEMENT Approved for public release. Distribution is unlimited.	**12b. DISTRIBUTION CODE** A

13. ABSTRACT (maximum 200 words)

Micro-electro-mechanical systems (MEMS) have been previously shown to be a viable option for radiation sensors requiring small, low-cost, and low-power designs. A resistive sensor combining boron-nitride nanotubes and multi-walled carbon nanotubes with an interdigitated electrode design printed with conducting ink can be used to detect thermal neutron radiation. This thesis explores how the initial resistance of the boron-nitride nanotube and multi-walled carbon nanotube mixture, which forms the connections across the printed conductive ink, influences the percent change in resistance of the sensor after thermal neutron exposure. The experiments will determine an ideal initial resistance that will produce the most sensitive resistor with ideal dynamic range. A key aspect of this research proved that the results of a resistor showing increasing resistance with neutron exposure are reproducible by comparing the results to work performed previously by the Naval Postgraduate School.

14. SUBJECT TERMS micro-electro-mechanical systems, MEMS, thermal neutrons, radiation nose, boron-nitride nanotube, carbon nanotubes	**15. NUMBER OF PAGES** 87
	16. PRICE CODE

17. SECURITY CLASSIFICATION OF REPORT Unclassified	**18. SECURITY CLASSIFICATION OF THIS PAGE** Unclassified	**19. SECURITY CLASSIFICATION OF ABSTRACT** Unclassified	**20. LIMITATION OF ABSTRACT** UU

NSN 7540-01-280-5500

Standard Form 298 (Rev. 2-89)
Prescribed by ANSI Std. 239-18

THIS PAGE INTENTIONALLY LEFT BLANK

Approved for public release. Distribution is unlimited.

MINIATURIZED NEUTRON RADIATION DETECTOR USING BORON-NITRIDE AND MULTI-WALLED CARBON NANOTUBES

Kyle M. Surovec
Lieutenant, United States Navy
BS, St Vincent College, 2013

Submitted in partial fulfillment of the
requirements for the degree of

MASTER OF SCIENCE IN APPLIED PHYSICS

from the

NAVAL POSTGRADUATE SCHOOL
June 2023

Approved by: Dragoslav Grbovic
Advisor

Craig F. Smith
Co-Advisor

Frank A. Narducci
Chair, Department of Physics

THIS PAGE INTENTIONALLY LEFT BLANK

ABSTRACT

Micro-electro-mechanical systems (MEMS) have been previously shown to be a viable option for radiation sensors requiring small, low-cost, and low-power designs. A resistive sensor combining boron-nitride nanotubes and multi-walled carbon nanotubes with an interdigitated electrode design printed with conducting ink can be used to detect thermal neutron radiation. This thesis explores how the initial resistance of the boron-nitride nanotube and multi-walled carbon nanotube mixture, which forms the connections across the printed conductive ink, influences the percent change in resistance of the sensor after thermal neutron exposure. The experiments will determine an ideal initial resistance that will produce the most sensitive resistor with ideal dynamic range. A key aspect of this research proved that the results of a resistor showing increasing resistance with neutron exposure are reproducible by comparing the results to work performed previously by the Naval Postgraduate School.

THIS PAGE INTENTIONALLY LEFT BLANK

Table of Contents

THIS PAGE INTENTIONALLY LEFT BLANK

List of Figures

THIS PAGE INTENTIONALLY LEFT BLANK

List of Tables

THIS PAGE INTENTIONALLY LEFT BLANK

List of Acronyms and Abbreviations

BNNT	Boron Nitride Nanotubes
C-C	Carbon-Carbon
CNT	Carbon Nanotube
eV	Electron Volt
MEMS	Micro-Electromechanical System
MWCNT	Multi-Walled Carbon Nanotube
PET	Polyethylene Terephthalate
PuBe	Plutonium Beryllium
SWCNT	Single Walled Carbon Nanotube
TLD	Thermoluminescent Dosimeter

THIS PAGE INTENTIONALLY LEFT BLANK

CHAPTER 1:
Introduction

Neutrons have long been regarded as a difficult form of radiation to detect. They are uncharged particles that have no direct ionizing capabilities and can only be detected by monitoring for the secondary charged particles or other reaction products (such as gamma radiation) resulting from neutrons interacting with matter. In addition, since neutrons have no charge, their interaction with matter is more difficult to predict theoretically and is generally characterized experimentally.

Following the discovery of the neutron by Chadwick in 1932 [1], neutron detection research has been a significant focus of scientific study, in the early stages driven by military research and the atomic bomb. Neutron detection has had incremental developments since the first proposed Helium-3 neutron detector in 1939 [2]. As technology has advanced, so has the need to produce ever evolving and more advanced ways for neutron detection. With the current radiation detection market expecting an increase in market value of 1.28 billion dollars by 2026 and increasing neutron producing technologies, the need for more accessible neutron radiation detection has become apparent [3].

This thesis will discuss a style of radiation detection that can be combined with other sensors to operate similar to a nose. The specific detector this thesis focuses on is solely for neutrons, but when combined with other detectors, the combination will be able to distinguish different types of radiation signatures and give levels of each just as a nose can distinguish between different smells. The technology of an electronic nose was first discussed in 1982 [4]. The electronic nose operates much like the human olfactory system, according to Wilson and Baietto in [5], "an electronic nose system typically consists of a multi sensor array, an information-processing unit such as an artificial neural network, software with digital pattern-recognition algorithms, and reference-library databases." The olfactory system's nose receptors and sensory neurons are replaced with processing units and algorithms designed to recognize specific types of radiation. This thesis will specifically focus on designing the neutron sensing unit.

A modern application for the idea of using receptors as a nose is mentioned in Han et

al. [6] at NASA Ames Research Laboratory, using polydimethylsiloxane (PDMS) as a gate dielectric in a metal oxide semiconductor field effect transistor. This thesis will expand on the ideas of Han et al. [6] and design and test a sensor using boron-nitride nanotubes (BNNT) in solution with multi-walled carbon nanotubes (MWCNT).

1.1 Applications for the Electronic Nose Detector

Micro-electro-mechanical systems (MEMS) provide the ability for radiation detection across a large range of fields, from medicine to homeland security and space operations [7]. With MEMS technology comes the ability to mass produce sensors with low-cost and a small footprint. Another advantage of MEMS in general, that is also applicable to this case, is the ability to seamlessly integrate with the readout electronics. MEMS allow the sensor to be made task-specific to conform with the required detection methods.

Dosimetry is an area that could greatly benefit from further advances in neutron detection. Personnel currently rely primarily on thermoluminescent detectors (TLD) to detect and quantify radiation exposure. TLD's are passive radiation dosimeters which rely on heating a sensitive crystal that has been exposed to radiation and measuring the intensity of the light emitted when heated. The intensity of light is proportional to the radiation dose received [8]. The downside of TLD's is that there is no live read out of the level of radiation the TLD was exposed to or the type of radiation responsible for the exposure. However, the application of MEMS to a dosimeter can combine the use of electromagnetic radiation-sensitive materials with low-power computing to produce an improved detection technique enhancing radiation detection for personnel [7]. The features of small size, low-cost and low-power consumption would allow combining such dosimeters with cell phones or other data recording devices for continuous monitoring.

Current neutron detection largely relies on gas proportional counters which utilize gases such as boron-trifluoride or helium-3 [7]. The mechanism of detection for these counters is the ionization of the gas from an incoming neutron as a result of its interaction with sensitive nuclei such as boron-10 or helium-3. However since neutron interactions are largely probabilistic collisions, the area required for suitable detection probabilities is large, popular gas detectors currently used are around 30 cm long [9]. Large-scale laboratories are able to use these counters, but this type of detection is unsuitable for personnel dosimetry.

Other applications of neutron detection as employed by the Department of Homeland Security at a total of 444 seaports throughout the U.S. is scanning for neutron emitting materials [10]. Some of the methods used for radiation detection at shipping ports are: drive-through radiation portal monitors, personal radiation detectors, radioisotope identifiers, and large-scale gamma ray/x-ray imaging systems [11]. The work done in this thesis could specifically aid the process for personal radiation detection and further down the line even radioisotope identifiers when combined with other radiation sensors.

1.2 Thesis Structure and Experimental Outline

The thesis consists of five chapters and one appendix that lay out the background and process taken to study and improve a MEMS-based radiation detector. It opens with an introduction and concludes with results and analysis. Chapter 2 (background) is an in-depth look into the physics of how carbon nanotubes (CNTs) and boron nitrate nanotubes (BNNTs) can be used for neutron detection starting from basic radiation principles. This chapter also discusses the physics behind carbon nanotubes and the properties taken advantage of for this MEMS detector. Chapter 3 discusses the detailed process of the MEMS detector fabrication and experimental methods. Chapter 4 lays out the results from the testing of the MEMS neutron detector and Chapter 5 offers a conclusion and recommendations on continued work. Appendix A presents additional figures showing the results of the IV characteristics of the fabricated sensors.

The actual exposure of the MEMS detector to neutron fluxes was done through a collaboration with Lawrence Livermore National Laboratory (LLNL). LLNL has access to neutron-emitting media, and has expertise in the safety and use of radioactive source materials. LLNL was instrumental in the experimental process and the gathering of data to support the findings of this thesis.

THIS PAGE INTENTIONALLY LEFT BLANK

CHAPTER 2:
Background

To be able to fully explain how this MEMS detector functions, an in-depth discussion of the basics of nuclear interactions with material is required. How the specific materials chosen for this detector interact, or do not interact, with neutrons is addressed on a broad conceptual scale. Then a closer analysis is presented on the details of how this detector utilizes specific properties of each material chosen throughout the fabrication process. Neutrons interact with material largely on a probabilistic basis and how the materials chosen increase this probability is discussed. Then the physics of how the detector works, aside from the nuclear interactions, is discussed focusing on how the CNTs form the changing resistive properties of the sensor. The information contained in this chapter as well as in the background presented by Hameed and Gats are the driving factors in the material selection for the detector [7].

2.1 Neutron Radiation

Neutrons are electrically neutral particles making them not subject to any electromagnetically-repulsive force hindering their interaction with an atomic nucleus. A neutron's interaction with a nucleus can be separated into four categories: elastic scattering, inelastic scattering, neutron absorption, and radiative capture [9]. Fissionable sources are able to absorb a neutron and then undergo a high energy splitting of its atomic nucleus. The ability of a source to absorb a neutron is quantified in its nuclear cross section for absorption which then results in some emitted particle or radiation (alpha particle, gamma, etc.). When the neutron is absorbed, the resulting nucleus undergoes a stochastic process of nuclear decay during which the energetic and unstable nucleus transitions to a stable state through emitting neutrons and other radiation products [12]. The creation of nuclear weapons relies on these emitted neutrons from some fissionable source then going on to be absorbed by other fissionable nuclei. This process happens many times over resulting in a tremendous release of energy. Similar to the release of energy from a fissionable source, although on a much lower scale, the detector studied in this thesis will also harness this energy release from Boron-10 after its interaction with a neutron.

2.1.1 Nuclear Cross Section

Neutron's interactions with a nucleus are probabilistic events. The nuclear cross section of an isotope is the measure of the probability that a neutron undergoes a certain interaction with that isotope, such as absorption, capture, scattering, etc. In other words, it is the effective area a nucleus presents to an incoming particle, in this case a neutron, for a particular type of reaction. This effective area is measured in barns (10^{-24}cm^2). Another important detail of a nuclear cross section, is an element's sensitivity to the energy of the incoming particle. Neutron capture is highly dependent on the energy of the incoming neutron because some nuclei are much more sensitive to certain energies than others, thus being "tuned" to these energies [13]. If a nucleus is more sensitive to a certain energy, its cross section for that reaction will be larger (increasing the effective area presented to the incoming neutron). In addition to the preference for interaction at particular energies (e.g. resonance capture), cross sections for many interactions are much higher at low (thermal) energies than at high (fast) energies.

For the detector studied in this thesis, the most important neutron reaction is the boron-10 (n,α) reaction. Boron-10 is an isotope of natural boron, is readily available, has a high neutron absorption and interaction cross section [7]. As to its availability, natural boron consists of roughly 80% boron-11 and 20% boron-10 by mass, but boron-10's nuclear cross section for the (n,α) reaction for thermal neutrons (neutrons with energy of approximately 0.025 eV) is roughly 3840 barns and boron-11 is 790 barns, nearly five times less [14] [7]. Figure 2.1 shows the nuclear cross section for the boron-10 (n,α) reaction and how it varies for incident energy of the neutron.

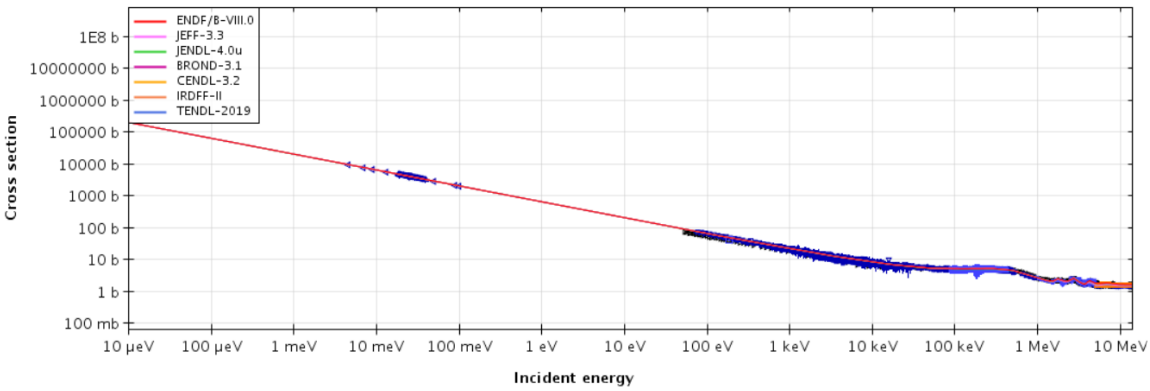

Figure 2.1. Cross section vs. incident energy for the boron-10 (n,α) reaction. Source: [14].

2.1.1.1 Neutron Capture, (n,α) Reaction

This detector will rely on the boron-10 atom within a boron nitride nanotube capturing a neutron and undergoing the (n,α) reaction. The boron-10 absorbs the neutron to form a short lived compound nucleus in an excited, unstable state. This new compound nucleus quickly de-excites by emitting an alpha particle (consisting of two protons and two neutrons), and gamma radiation and then forms a final lithium-7 nucleus. Equations 2.1 and 2.2 show the reactions; the difference between the two is that 94% of the time, the lithium atom is excited (represented by $Li^{'}$) and de-excites by emitting gamma radiation, and 6% of the time the lithium product is not in an excited state.

$$^{10}_{5}B +^{1}_{0} n \rightarrow^{7}_{3} Li +^{4}_{2} \alpha + 2.79\,\text{MeV}(6\%) \tag{2.1}$$

$$^{10}_{5}B +^{1}_{0} n \rightarrow^{7}_{3} Li' +^{4}_{2} \alpha + 2.31\,MeV + \gamma(0.48MeV)(94\%) \tag{2.2}$$

In the 94% probability case, the excited lithium atom quickly decays to the ground state emitting a gamma ray of 0.48 MeV in 10^{-13} seconds. The incoming thermal neutron has energy of ~0.025 eV, contributing negligibly to the total energy balance of the reaction. The kinetic energies of the products can then be determined using conservation of momentum (assuming that the alpha particle and the lithium atom are emitted in opposite directions).

$$E_{Li} + E_{\alpha} = 2.31 MeV \tag{2.3}$$

$$\sqrt{2m_{Li}E_{Li}} = \sqrt{2m_{\alpha}E_{\alpha}} \tag{2.4}$$

Solving the two equations results in a yield energy of 0.84 MeV for the lithium atom and 1.47 MeV for the α particle [15]. Some of the subsequent collisions, especially those involving alpha particles will inevitably strike the nanotubes. If the strike results in the severing of the nanotube, one fewer conductive pathway is available, which results in reducing the conductivity (increasing the resistance) of the mixture. Additionally, some of this energy is turned into heat as these collide with surrounding matter which could be causing secondary effects on the resistance of the sensor.

2.2 Detector Physics

The MEMS detector designed for this thesis will rely on the conductivity of a CNT/BNNT mixture resistor changing when exposed to the neutron radiation. The resistive sensor will combine the material properties of CNTs and BNNTs; CNTs for its conductive properties and BNNTs for their sensitivity to neutron radiation. The two materials combined together form the basis of the resistive sensor.

2.2.1 Structural Properties of Carbon Nanotubes

Single walled carbon nanotubes (SWCNT) were first studied in the early 1990s. Sumio Iijima published a paper in 1991 on the successful creation of the SWCNT [16]. Prior to this, helical carbon nanotube structures were known to exist, but were thought of as a biproduct of other processes without use [17]. With Iijima's research, SWCNTs were shown to be useful across a vast range of applications benefiting a wide variety of fields which previously thought them not useful [7], [17].

Similar to a plane of graphene, SWCNTs lattice sturcture is filled with sp2 hybridized carbon atoms. However unlike graphene which is a two dimensional plane, SWCNTs take this lattice structure and roll it to a diameter of a few nanometers, then cap the ends with

hemi-fullerenes [17]. The lattice is typically a repeating hexagonal pattern, with many possible variations in the morphology that can amplify the various aspects of the nanotubes material properties, such as thermal and electrical conductance [7]. The many ways to form the nanotube can be thought of by rolling a piece of paper. Depending on where you start rolling will determine how the paper rolled will look. For example, if you start by grabbing the center of the side, the paper rolled up will look different than if you started rolling from a corner. Like this analogy, the CNT has many different variations on how it can be rolled, and each different way will change the structure of the nanotube. A way to consider the structure of the unit cell of a CNT is in terms of the direction vectors, or chiral vectors. The chiral vector is defined by integer numbers of two unit vectors ($a_1$and a_2) as shown in Figure 2.2.

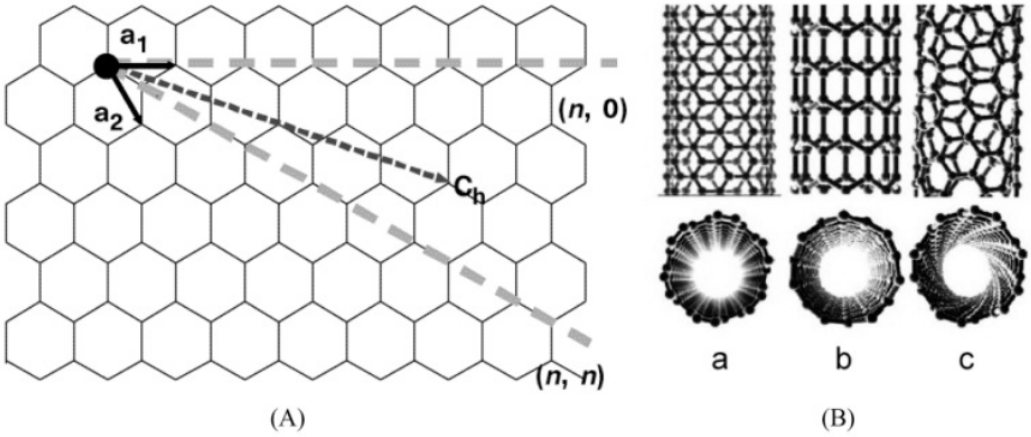

Figure 2.2. (A) The chiral vector of a carbon nanotube in a two dimensional graphene; (B) Molecular models of single-walled carbon nanotubes: armchair (a), zigzag (b), and chiral (c). Source: [18].

The geometry of the SWCNT is defined then by the integer number of chiral vectors. If m equals the number of a_1 unit vectors and n equals the number of a_2 unit vectors, armchair nanotubes are formed when m = n, zigzag when m or n is zero, and all other configurations are chiral [19]. The hexagonal structures (governed by the values of m and n) of each arrangement will determine the electrical properties of the SWCNT, even though the number of bonds and the element remains the same. The width of the nanotube is on the order of nanometers, thus the electronic properties will be defined by the quantum

confinement of the electrons along the diameter of the nanotube. Propagation of electrons only occur along the axis so the one dimensional band structure will depend on the standing waves developed around the circumference of the nanotube [19]. Calculations done on the band structure of SWCNTs, presented by White in Physical Properties of Materials, "show that an (m,n) carbon nanotube will be metallic when m - n = 3I, where I is an integer." [19] Therefore, according to the rules described above in the naming convention of the lattice structures, armchair nanotubes are metallic, a third of the zigzag nanotubes are metallic, and the remaining (two thirds of the zigzag and all the chiral) are semiconducting [19].

Multiwalled carbon nanotubes (MWCNT) are similar to SWCNTs but can have two possible arrangements of SWCNTs; a 'Russian Doll' or 'Swiss-roll' structure. The differences in the structures are pictured in Figure 2.3. Experimental studies have shown that the 'Russian Doll' configuration is more likely, at least for MWCNTs produced by arc-evaporation [20] (the process used to produce the MWCNTs used for this thesis).

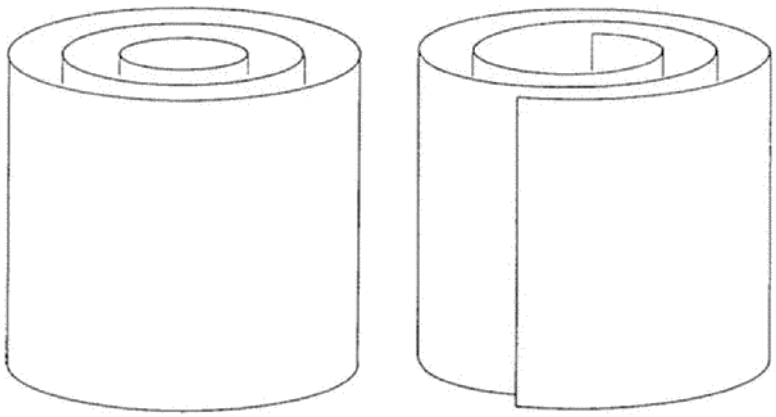

Figure 2.3. Representation of a Russian Doll (figure on the left) and Swiss Roll (figure on the right) structure of MWCNTs. Source: [20].

The arrangement of the hexagonal structures can still only be armchair, zigzag, and chiral with different spacing in between successive rolls for each configuration. The inter-tube distance can be as low as 0.352 nm. This is limited by the fact that the difference in circumference cannot be less than 0.246 nm which is the width of one hexagon [20].

2.2.2 Electrical Properties of Carbon Nanotubes

Much of the electrical properties of SWCNTs and MWCNTs has come from extrapolation of studies on the electronic structure of graphite. This was then used as the basis for the theory on MWCNTs and SWCNTs. In plane mobility of MWCNTs is high with an in-plane resistivity of 0.4 $\mu\Omega$ m, with comparatively low mobility perpendicular to the planes (anisotropic mobility) [20]. The band overlap of three dimensional graphite was discovered in the 1950s to be approximately 40 MeV implying that graphite is a semi-metal with free electrons and holes regardless of temperature [20]. However, graphite has a carrier density of roughly 10^{18}cm^{-3}which is about one carrier per 10^4 atoms, 4 orders of magnitude lower than carbon which has one free charge carrier per atom. Despite having a low density of charge carriers, the carrier mobility is relatively high in the basal plane, offsetting the low density of charge carriers when considering the electrical conductivity of graphite [20].

The band structure data for graphite was theorized by introducing macroscopic boundary conditions to an infinite graphene plane. Taking this theory and modify it for CNTs, the fiber axis is still a macroscopic dimension with few limits on the allowed states, but the circumference is at the atomic level, meaning the circumferential allowed states will be limited [20].

The MWCNTs used in this detector are a semiconducting graphene structure with a direct band gap (~1 eV) allowing for more rapid radiation detection [7]. The uncertainity in the density of states in MWCNTs leads to the uncertainty in the band gap. Figures 2.4 and 2.5 show how changing the structure of a zigzag CNT from (9,0) to (10,0) vastly changes the density of states. In accordance with the chiral vector rules presented by White [19], the (9,0) tube is metallic as shown by its non zero density of states at the Fermi level, while the semiconducting (10,0) tube has zero density of states at the Fermi level.

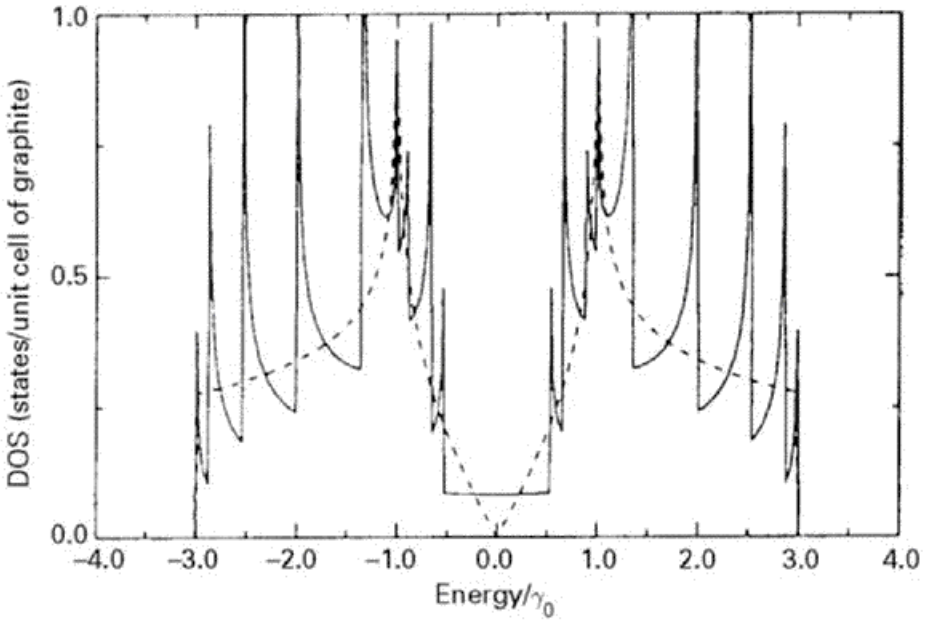

Figure 2.4. 1D density of states for a (9,0) zigzag metallic tube. Source: [20].

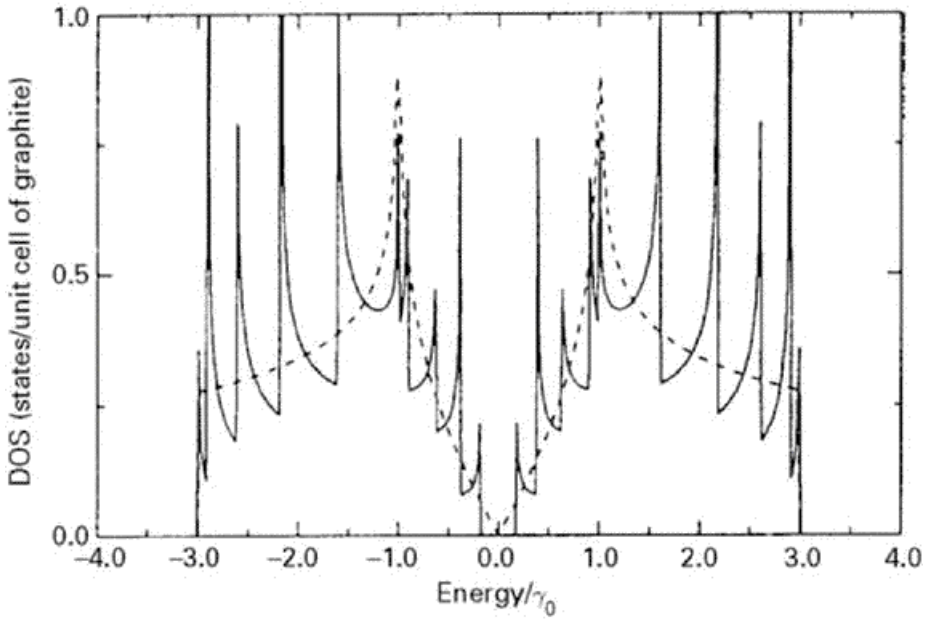

Figure 2.5. 1D density of states for a (10,0) zigzag metallic tube. Source: [20].

As discussed, the electronic states in a carbon nanotube will be very limited, resulting in the transport of electrons in a metallic nanotube to be essentially that of a quantum wire. Electron transport appears to be diffusive rather than ballistic, however experimentation has found very high mobilities in semiconducting nanotubes. Additionally, since the conduction will only occur in discrete, well separated states, resistance and the length of the tube will not change proportionally, or even consistently [20].

Resistance measurements on MWCNTs were first performed in 1996 by experimenting on a single MWCNT supported by an oxidized silicon wafer. These early experiments found that resistance increased with decreasing temperature, indicating that the MWCNT was semiconducting [20]. Later, additional testing was done by the NEC. They first annealed the nanotubes to remove any defects, then connected a nanotube to four 80 nm wide tungsten wires as shown in Figure 2.6.

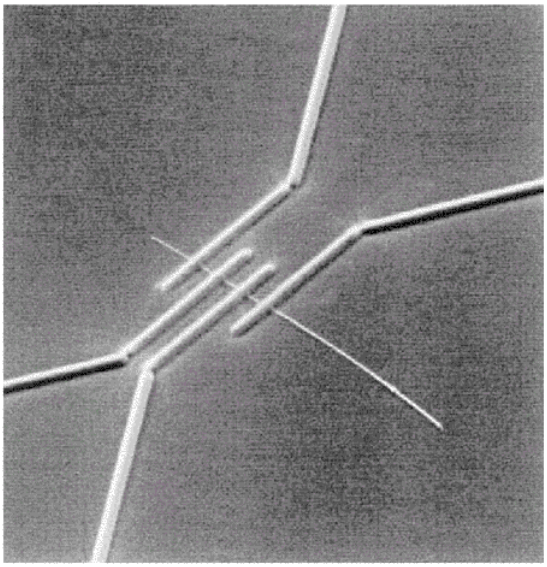

Figure 2.6. Focused ion beam image of a single MWCNT connected to four tungsten wires which are 80 nm wide. Source: [20].

When eight different nanotubes were measured with this configuration, the resistances varied widely as well as the dependence on temperature. Resistivities varied from 8 mΩ m to 0.051 μΩ m for nanotubes ranging from 10 nm to 18.2 nm diameter (lower than that of in plane graphite which is 0.4 μΩ m) respectively [20]. The resistance of the 18.2 nm wide MWCNT

was 200 Ω across a 1.0 μm gap. The nanotubes used for this thesis are on average around 20 nm wide, so the resistances and resistivities used were the values listed for the 18.2 nm wide nanotube. In these experiments, all tubes showed a slight decrease in resistance with increasing temperature, however, the consensus is that this is not due to semiconducting properties. Instead, the tubes are thought to be essentially metallic, with the variance in the resistance being from changes in charge carrier concentration and mobilities [20]. These wide variance in resistivities suggest that the geometry of the nanotube plays a profound role in determining its electronic behavior.

In Chapter 3, an analysis is done on the estimated number of nanotubes forming the connection across the interdigitated fingers of the resistor. However, due to the difficulty in measuring the resistance of a single nanotube as presented by Harris [20], these calculations are rough estimates to get an idea on the order of magnitude of the number of nanotubes forming the connection.

2.2.3 Mixing Carbon Nanotubes

Carbon nanotubes can form a suspension in water but the degree of dispersion is difficult to quantify since the dispersion state changes over time [21]. Two terms have been defined for CNT suspension; macrodispersion and nanodispersion. Macrodispersion is the dispersion of aggregates of carbon nanotubes while nanodispersion is individual carbon nanotubes being suspended in solution [22]. For the purposes of this thesis, the CNTs will be macrodispersed in water prior to being deposited on the printed interdigitated fingers. Two general processes have been typically used for dispersing CNTs; chemical and mechanical. Chemical methods involve using solvents, solvent compositions, or solvent additives such as surfactants. However, the most popular method and the one used in this thesis is mechanical by means of ultrasonication. Hydrophobic forces and van der Waals attraction up to 950 eV/μm between CNTs cause them to aggregate in water [23]. Due to these forces, energy has to be added to the CNTs in the solution in order to break these forces via ultrasonication. The same process of ultrasonication can be used to break the van der Waals forces in the BNNTs.

2.2.3.1 Ultrasonication

For this thesis work, ultrasonication is the chosen mechanical dispersion technique due to its ability to reduce the size of the CNT aggregates [22]. Ultrasonication is the process by which sound energy with a frequency in excess of 20 kHz is used to agitate particles, in this case for mixing CNTs and BNNTs in water. Ultrasonic probes (transducers) are used to produce acoustic cavitation. The cavitation produced by intense sonication creates energy-dense conditions with high temperature and pressure as well as high shear forces and turbulence. These intense conditions can agitate particles resulting in homogenization, dispersion, and other effects.

Sonication does involve some risk to the CNT integrity. Complex physical and chemical processes can occur that if not accounted for can cause adverse alterations to the structure of the CNTs. Over-sonication and under-sonication can frequently occur if adequate attention is not paid to the process of sonication. Over-sonication results in the breakage of the CNT structure and under-sonication will not result in an adequate dispersion. Zaib and Ahmad [22] reported on a process for optimizing sonication parameters to obtain dispersion of the nanotubes in water. They varied multiple parameters, such as amplitude and pulse on-off time. Pulse off time was unexpectedly important, even more so than total sonication time, which carried the minimum weightage in their models. Figure 2.7 shows a pareto graphic of relative importance of the sonication parameters.

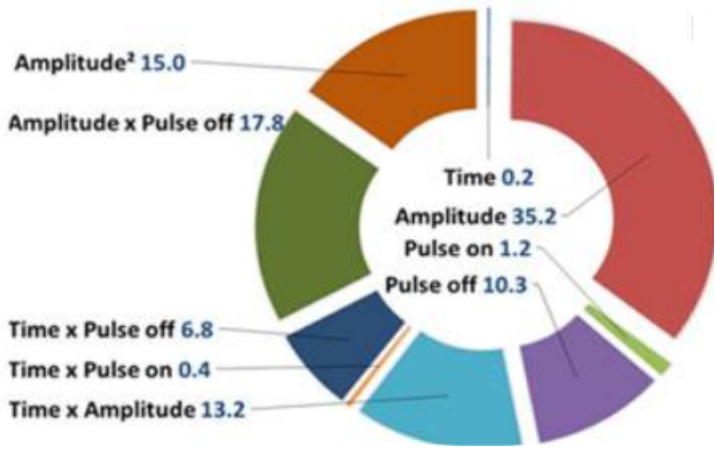

Figure 2.7. Pareto graphic analysis of a sonicator's operational parameters that influence the distribution of MWCNT aggregates. Source: [22].

2.2.4 Properties of Boron Nitride Nanotubes

Boron nitride nanotubes are similar to carbon nanotubes in their lattice and design, but with alternating boron and nitrogen atoms instead of carbon in their hexagonal lattices, as shown in Figure 2.8. Dark sites represent the boron atoms and light sites are the nitrogen atoms. Energy constraints on the configuration and the restrained morphology cause the alternation of the boron and nitrogen atoms [7]. BNNTs are high aspect ratio rod-like nanostructures, microns long, diameters on the order of nanometers, and are thermally conductive, electrically insulating, neutron shielding, and piezoelectric [24]. Unlike carbon nanotubes, the BNNTs are electrically insulating and are able to maintain their thermal and chemical properties in a 900 degree Celsius environment [24].

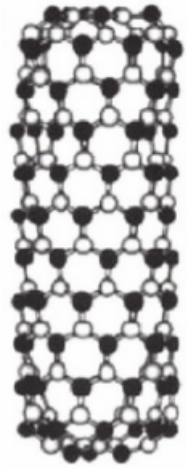

Figure 2.8. Hexagonal BNNT. Source: [7].

Pure boron-10 is used for the detector because of its high nuclear cross section as discussed in Section 2.1.1. Hexagonal morphology boron-10 is used for the nose detector because of its ease of procurement, and the decay products resulting from neutron radiation shown in equation 2.1 and 2.2. The BNNTs have a low electrical conductivity, making them better insulators, so these nanotubes will contribute solely to changing the resistance of the detector by breaking the CNTs by the emitted alpha particles from the neutron capture reaction. The boron-10 will be used in nanotube form for ease of mixing with the CNTs.

2.2.5 Nanotubes as a Resistor

In conclusion on how the nanotubes will be used as a resistor, the CNTs will form the connection across the interdigitated finger electrodes to form the resistor, with BNNTs mixed in prior to deposition on the electrode. The detection mechanism is designed as a solid-state scintillator. Neutron irradiation will cause the boron-10 to undergo the neutron capture reaction, emitting a high energy alpha particle, as well as other products. The alpha particle will then probabilistically hit a carbon-carbon (C-C) bond in the CNTs. Since the C-C bond have a bond strength of 3.6 - 3.9 eV [7], the alpha particles, with an energy of 1.47 MeV, should destroy the C-C bonds, creating defects in the CNTs and/or breaking the nanotube connections completely, inhibiting the flow of electrons and causing an increase in resistance.

THIS PAGE INTENTIONALLY LEFT BLANK

CHAPTER 3:
MEMS Sensor Fabrication and Experimental Methods

3.1 Design of the Interdigitated Electrodes

The design of the interdigitated electrodes used in this thesis are based on the work of Hameed and Gats [7] and their work with NASA. The sensor supplied by NASA is shown in Figure 3.1. An interdigitated electrode design is used to increase the density of MWCNT connections across the two electrodes. The electrodes are connected to two larger pads for ease of measuring the resistance across the resistor once the BNNTs and MWCNTs are deposited. To construct the NASA sensors, a chemical sintering process was used prior to printing the resistor on transparency [7]. However this process was not used to fabricate the sensors developed for this thesis.

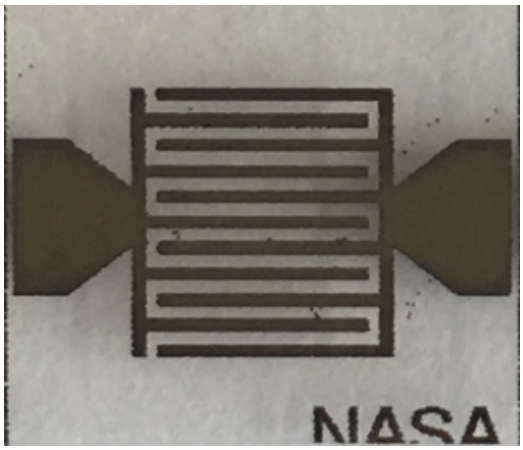

Figure 3.1. NASA Interdigitated Finger Electrodes. Source: [7].

An EPSON ST-M1000 ink jet printer was used to print a sensor modeled after the NASA sensor. The electrodes were printed using a Novacentrix Metalon® JS-B25P nanosilver electrically conductive ink designed to produce circuits on substrates. The ink is 25 wt% silver with an average nanoparticle size of 60-80 nm. Since the EPSON inkjet printer can only print as small as one pixel, Microsoft Paint was used to draw the electrodes in order to comply with the minimum size the printer could handle. The electrodes were printed on

a sheet of Novelle^{TM} (a polyethylene terephthalate (PET) sheet with a microporous inkjet receptive coating). The electrodes shown in Figure 3.2 were printed using the materials described above. Different geometries were printed in order to test if the electrode size of the resistor or the size of the gaps in between the interdigitated electrodes affected the performance of the sensor.

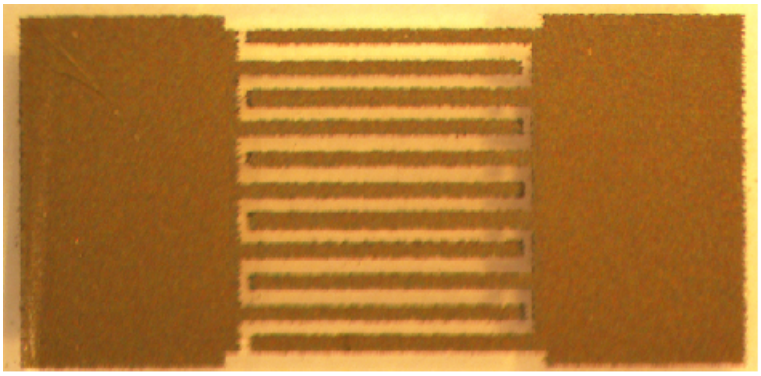

Figure 3.2. NPS designed interdigitated electrodes printed with the EPSON ST-M1000 printer

3.2 Estimating MWCNT Connections

Since the mechanism for neutron detection will be the changing resistance, resulting from disrupting the MWCNTs, an estimate of the number of connections is necessary. The gap between the interdigitated electrodes is 0.45 mm for the narrow gap and 0.91 mm for the wide gap. From Chapter 2, the resistance of a single MWCNT of a roughly 20 nm diameter was 200 Ω over 1.0 μm. This results in 9 x $10^4\Omega$ across the gap of the narrow gap electrodes and 1.8 x $10^5\Omega$ for the wide gap. The connections across the interdigitated electrodes are assumed to be resistors arranged in parallel. The MWCNTs are realistically not only making connections perpendicular to the nanotubes, but are crisscrossing across the gaps making contact with many nanotubes simultaneously. It is also likely that a single nanotube is not sufficient to bridge the complete length of the gap. However, even if multiple nanotubes contact each other in such a way to form a connection across the gap, they will collectively behave as a series of resistors. This configuration is called percolation [25]. Therefore, multiple connected nanotubes will behave as a single nanotube of the combined length (as shown in Figure 3.3).

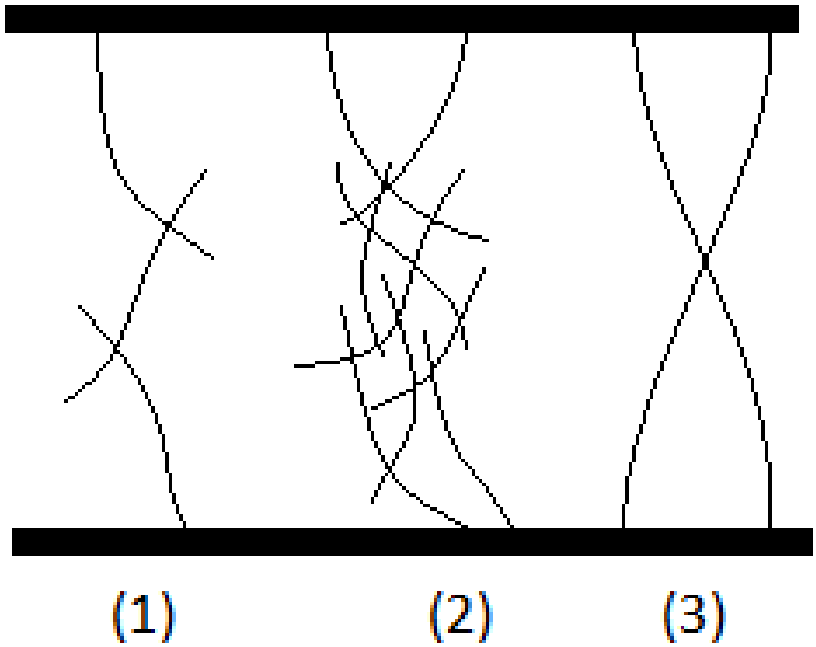

Figure 3.3. Thick solid lines are representation of the printed interdigitated electrodes. Thin lines are a representation of the CNTs making the connections across the interdigitated electrodes. (1) represents only a few CNTs making the connections whereas (2) represents many CNTs combining to make the connection. (3) is an example showing how in this arrangement the connection can be treated as two separate resistors in parallel.

If one nanotube is broken, it is hypothesized that this will be similar to removing a resistor from a parallel circuit. To calculate the number of connections, the total resistance of the sensor was used as the equivalent resistance then equation 3.2 was used to calculate the number of connections. All MWCNT bridges across the gaps were assumed to be the same length, simply the length of the gap, so all resistances of individual connections were assumed the same.

$$\frac{1}{R_{eq}} = \sum \frac{1}{R_n} \tag{3.1}$$

where R_n is the individual resistance of one MWCNT connection across the gap and R_{eq} is the equivalent resistance (the measured total resistance of the sensor) . Since all connection bridges were assumed to have the same resistance, equation 3.1 can be simplified to

$$\frac{1}{R_{eq}} = \frac{n}{R} \tag{3.2}$$

where n is the total number of connections. The number of nanotube pathways is then given by

$$n = \frac{R}{R_{eq}} \tag{3.3}$$

Note however that this is a simplified estimate which assumes that all of the nanotubes are of the same kind/resistance and of the same length (length of the gap).

3.3 MWCNT and BNNT Mixing

As explained in Chapter 2, mixing MWCNTs to achieve an adequate dispersion is best accomplished by ultrasonication. Hameed and Gats with the help of NASA observed that using a 10 mg of BNNTs and 1 mg of MWCNTs to 10 ml of water showed a changing resistance in the sensors when exposed to thermal neutrons [7]. To be able to compare results with Hameed and Gats, the sensors made for this thesis use the same concentrations of BNNT and MWCNTs. The first step in the ultrasonication process was to mix the BNNTs shown in Figure 3.4 produced by BNNT, LLC in bundles (having the consistency of cotton balls), with the 10 ml of water.

Figure 3.4. BNNTs received from BNNT, LLC

The BNNTs were also statically attracted to anything that came into contact with them, making separating them and accurately weighing them difficult. The 10 mg of BNNTs were added to a 50 ml glass vessel containing 10 ml of water. This mixture was then ultrasonicated with the ultrasonic probe driven by the Misonix Sonicator 3000 shown in Figure 3.5.

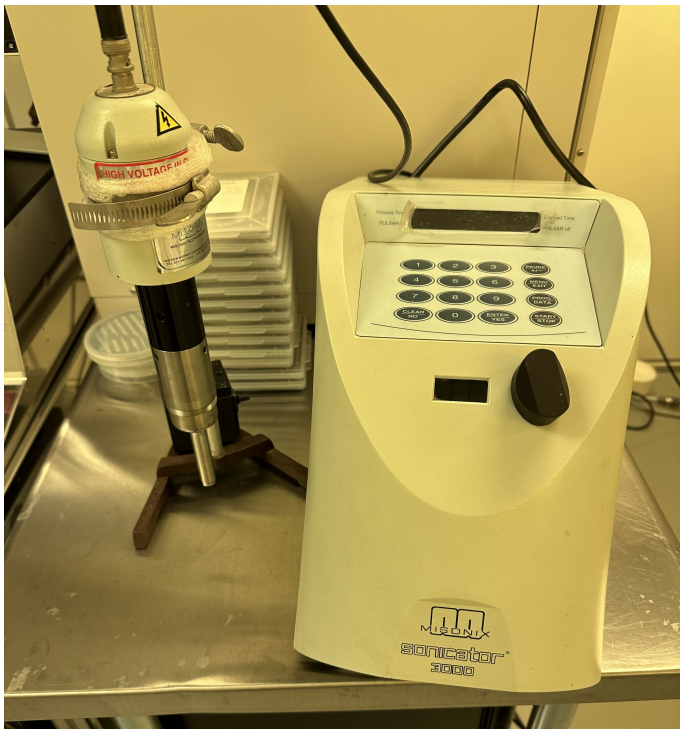

Figure 3.5. Misonx Sonicator 3000 with attached ultrasonic probe

BNNTs are difficult to work with due to being hydrophobic and not dispersing well in water [26]. To achieve an acceptable dispersion, the ultrasonic probe was driven at 36 W of power for 20 minutes with an on/off time of 20/40 seconds resulting in 1296 J/ml of energy used. This was able to achieve an adequate dispersion of BNNTs, but the dispersion was not stable. Within 5 minutes, the BNNTs were noticeably forming back into larger aggregates but better dispersion was not achievable by sonicating for a longer period of time or with a higher energy. Once the BNNTs were dispersed in water, 1 mg of MWCNTs were added to the solution. Sonication parameters were modeled after Zaib and Ahmad's conclusions [22]. A pulse on/off cycle of 44/30 seconds for a total mixing time of 88 seconds with an amplitude of 51 Watts expended 448.8 J/ml of energy. They found that the amplitude of the sonicator contributed over 75 % towards dispersing the MWCNTs, with the on\off time being of second most importance [22].

With the CNTs and BNNTs dispersed in solution, the solution was deposited onto the printed sensor using a 2 µL pipette. This process had to be completed quickly before the BNNTs

had a chance to form back into larger aggregates. The sensor then rested until the water had evaporated. All sensors had increasing resistance while the water was evaporating for an average of 30 minutes, at which point the resistances stabilized. Hameed and Gats [7] found that heating the sample to speed the process of evaporation permanently and dramatically increased the resistance between the electrodes, so the sensors built for this thesis were left at room temperature for evaporation.

3.4 Experimental Methods

Neutrons from various sources were used to test the sensitivity of the sensors built. All neutron radiation was performed in collaboration with and using the facilities of LLNL. To first recreate the results of Hameed and Gats and then to find an ideal initial resistance for maximum sensitivity, the sensors were exposed to various levels of radiation with their resistances measured before, and after their exposure, as well as continually during the exposure using an Arduino Uno board. The Arduino board was programmed to read resistance every second during the exposure using a simple voltage divider circuit with a 1 kΩ resistor. Figure 3.6 shows a schematic of the circuit with the Arduino board.

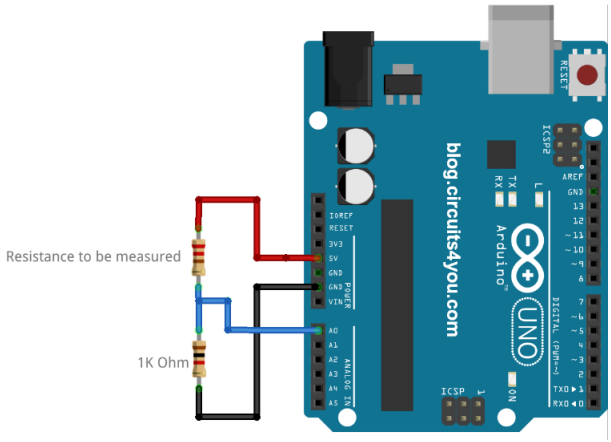

Figure 3.6. Arduino Board with simple schematic of voltage divider used to measure resistance of the MEMS sensor. Source: [27].

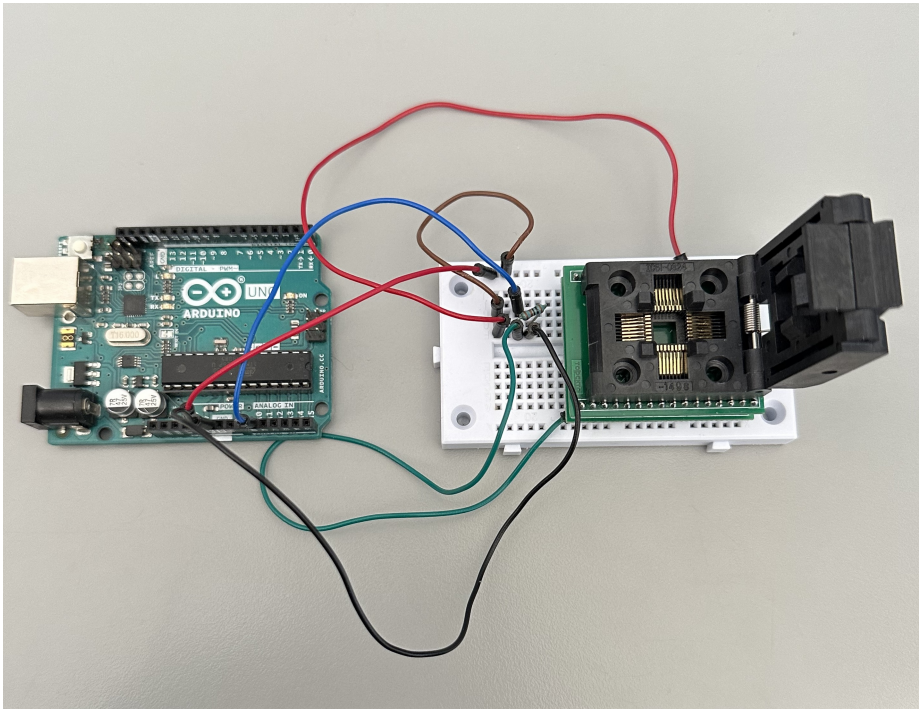

Figure 3.7. Arduino board connected to chip test socket. Electrical pads can be seen inside the holder that make contact with the two sides of the MEMS sensor

To attach the MEMS neutron sensors into the circuit in Figure 3.6, a plastic holder with multiple contact pads was connected to a bread board, and then connected to the Arduino board as shown in Figure 3.7. The measured extra resistance of the circuitry used to contain the holder was 8.7 Ω. In addition to measuring resistance with the Arduino Board, a standard multimeter was used to measure the resistance before and after exposure. Once the fabricated MEMS sensor was placed into the holder, the portion of the circuitry located on the bread board was exposed to neutrons generated by Californium 252 (Cf-252) and PuBe sources. The source was held at different distances and different levels of moderator were used in order to achieve different fluences of thermal neutrons. Table 3.1 shows how the neutron fluences change with the different moderators, distances from the source, and strength of the source. Additionally, Figures 3.8, 3.9, and 3.10 show the neutron spectra for Cf-252 sources with 5 cm, 10 cm and 15 cm of polyethylene at 2.0 m, 4.5 m, and 4.5 m respectively for comparison. Figure 3.11 shows the neutron spectrum for the PuBe

source. This source's unmoderated neutron spectrum is shown as opposed to the moderated (thermalized) spectrum of the Cf-252 sources.

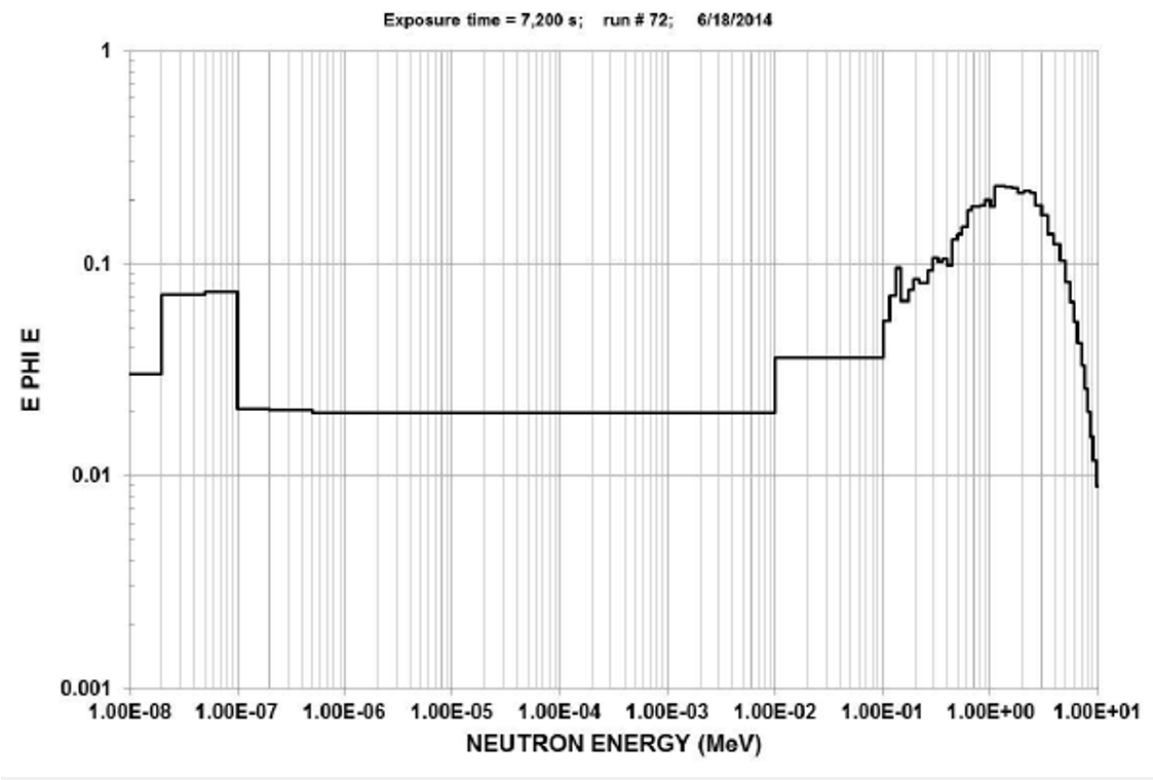

Figure 3.8. Neutron spectrum (Thermal - 10 MeV) at 2.0 m from Cf-252 source moderated by 5 cm radius HD polyethylene sphere

Table 3.1. List of sources used to expose MEMS sensor to neutrons. Also listed are the different amount of moderator used and the distance from the source. The moderator will heavily influence the amount of neutrons that reach a thermal energy prior to interacting with the MEMS sensor.

Source	Medium Cf-252	Medium Cf-252	Large Cf-252	Large Cf-252	PuBe-239
Moderator	15 cm poly	5 cm poly	5 cm poly	5 cm poly	10.16 cm poly
Distance from source	450 cm	200 cm	200 cm	100 cm	14.33 cm
Thermal Flux $\left(\frac{n}{cm^2 s}\right)$	28	67	1490	5959	194
Thermal - 4.5 MeV Flux $\left(\frac{n}{cm^2 s}\right)$	69	424	9491	37963	1938

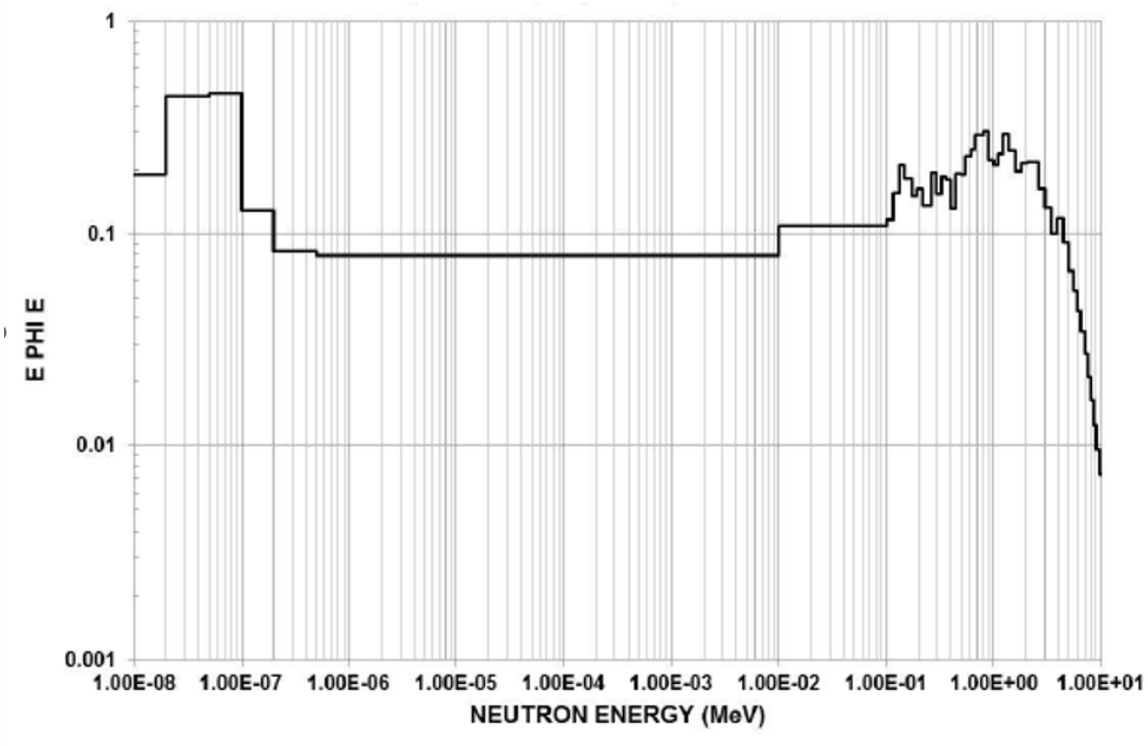

Figure 3.9. Neutron spectrum (Thermal - 10 MeV) at 4.5 m from Cf-252 source moderated by 10 cm radius HD polyethylene sphere

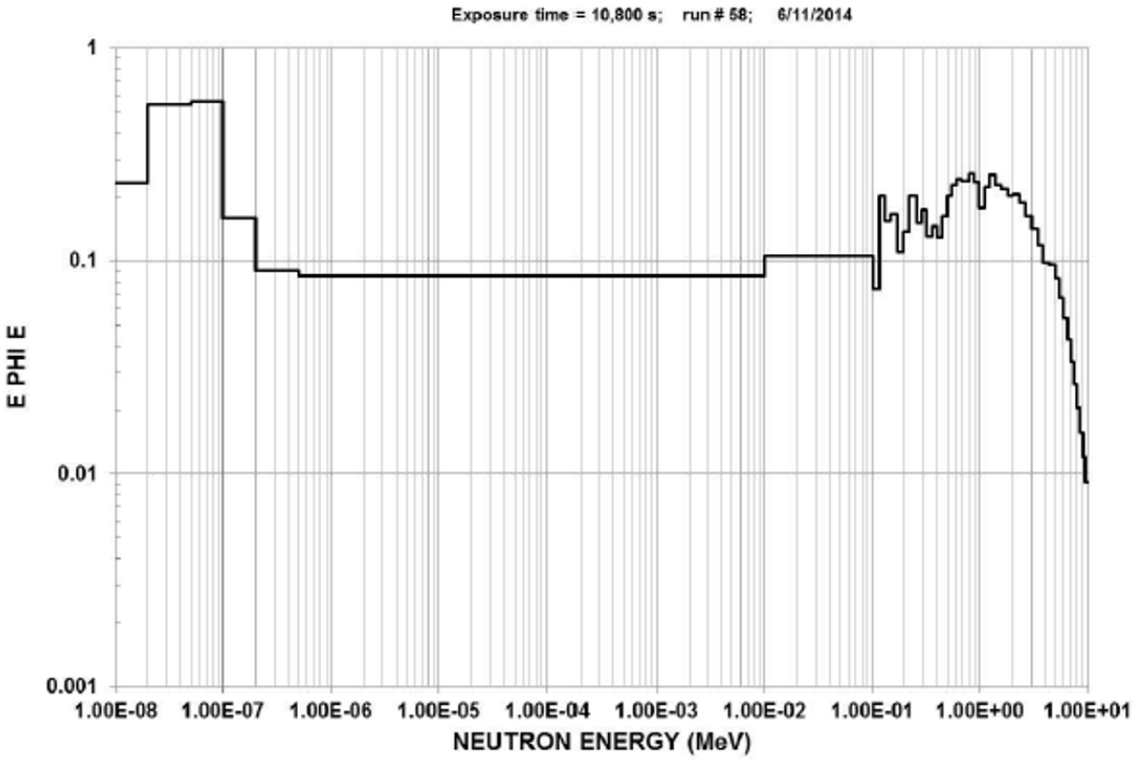

Figure 3.10. Neutron spectrum (Thermal - 10 MeV) at 4.5 m from Cf-252 source moderated by 15 cm radius HD polyethylene sphere

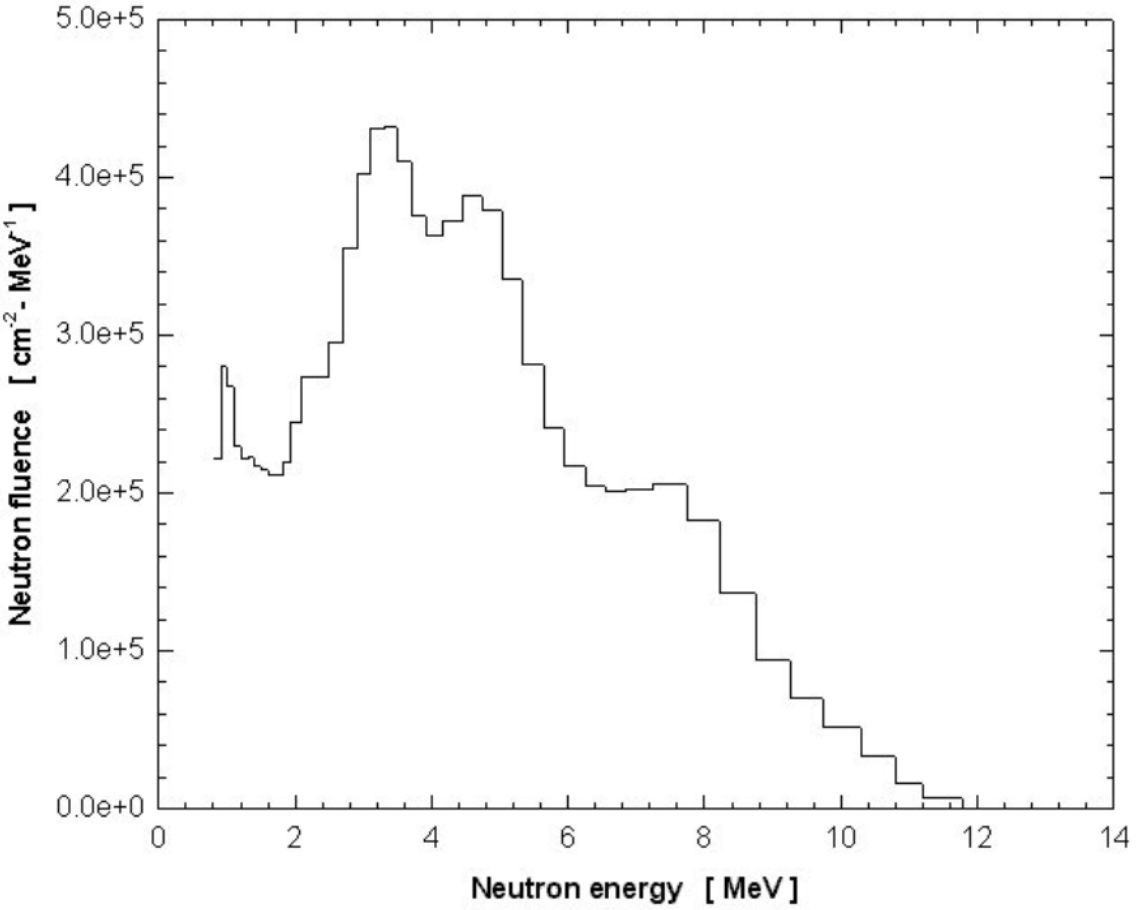

Figure 3.11. Neutron spectrum from a PuBe-239 source. Source: [28].

An exposure time of ten minutes was chosen in order to be able to compare results with Hameed and Gats [7]. Equation 3.4 was used to calculate the neutron flux from the various sources

$$\Phi = \frac{S}{4\pi d^2}\left[\frac{\mathrm{n}}{\mathrm{cm^2 sec}}\right] \tag{3.4}$$

where Φ is the flux, S is the strength of the neutron source, and d is the distance from the source. Each sensor had a slightly different size of deposited nanotube mixtures. By measuring the size of the deposited nanotube bundle and also by accounting for the total

exposure time, the total amount of neutrons that traveled to the CNT/BNNT mixture can be calculated. The exposures in terms of thermal fluence of each sensor are shown in Table 4.2.

The goal of this thesis is investigate the link between initial resistance and the change in resistance after neutron exposure. Each resistor has a different ratio of BNNT to MWCNT connections, which should result in different initial resistances as well as potential responses to exposures. Then after exposure, the percent change in resistance will be calculated and analyzed to see which resistance range results in the largest percent change in resistance. With this knowledge, different sensors could be built for different applications; the sensors sensitivity could theoretically be controlled by the amount of BNNTs and MWCNTs deposited.

CHAPTER 4:
Results

This chapter presents the results and data analysis from the exposure of the fabricated sensors to neutrons at LLNL. The experimentation involved exposing the sensors described in Chapter 3 to the neutron radiation generated by the sources in Table 3.1.

4.1 Initial Resistance Measurements

As described in Chapter 3, the BNNT and MWCNT solution was deposited on the printed sensor using a 2 μL pipette. Table 4.1 shows the initial resistances of the eight sensors fabricated for this thesis. Each resistor was given a name based on the organization that printed the electrodes as well as a numeric indicator in order to differentiate them.

Table 4.1. List of fabricated sensors with amount of nanotube solution deposited as well as initial resistance

Resistor	Solution Deposited (μL)	Initial Resistance (kΩ)
NASA1	2.5	59.75
NASA2	2.5	1.582
NASA3	2.5	1.634
NPS1	2.5	6.94
NPS2	2.5	2.45
NPS3	7.5	45.84
NPS4	7.5	10.14
NPS5	2.5	638

The initial resistances varied widely, even for the ones with the same nominal amount of nanotube solution deposited (as measured by the number of 2 microliter droplets). A reason for this could be that the pipette had a difficult time drawing solution into its nozzle. Another reason could be that not all of the nanotubes in the mixture end up being a part of one of

the percolation pathways connecting the two electrodes. Although the amount of nanotubes deposited was not noticeably different, getting the nanotubes to deposit consistently in the same position on each resistor proved impossible with the pipette. Since the resistance is going to be formed by making connections across the electrodes of the nanotubes, depositing those nanotubes in a different geometry on the printed electrodes will result in a different resistance if the number of connections across the electrodes is different. Also, since the BNNTs can start forming larger aggregates again and Van der Waals forces will attract MWCNTs to these larger BNNT aggregates, depositing a consistent amount of the solution is difficult. Two of the sensors after nanotube deposition are pictured in Figures 4.1 and 4.2 respectively. The MWCNTs can be clearly seen due to their black color, however the BNNTs cannot be seen. When grouped together as they come from the manufacturer, they have a white appearance but when mixed in with the MWCNTs, they are nearly translucent.

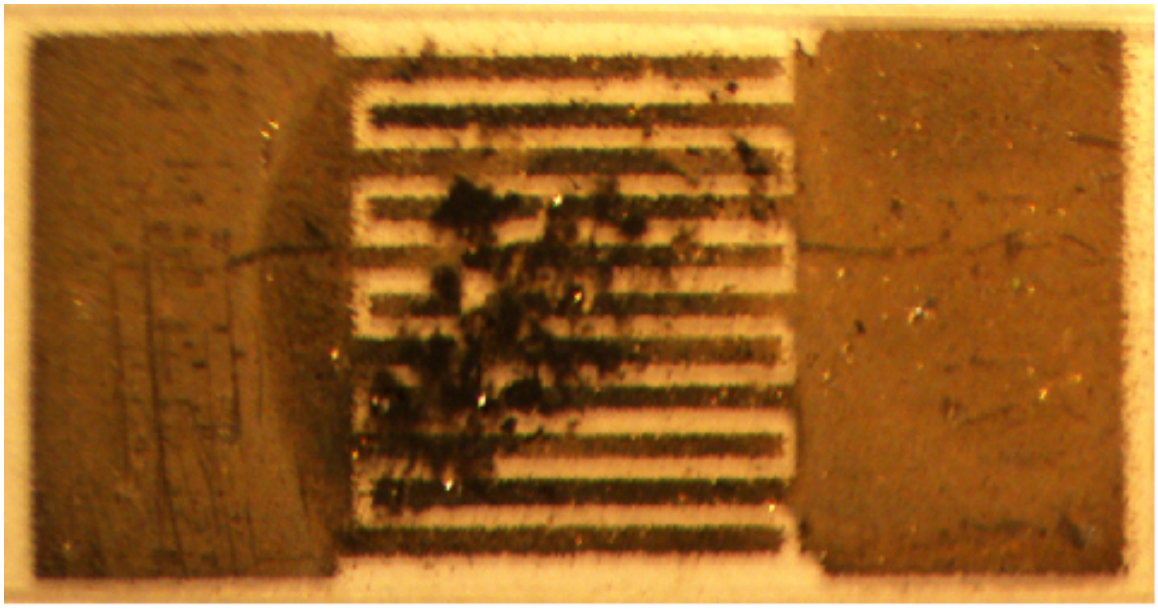

Figure 4.1. Complete BNNT and MWCNT sensor (NPS1). The carbon nanotubes are clearly visible however, due to their color the BNNTs cannot be seen in the image

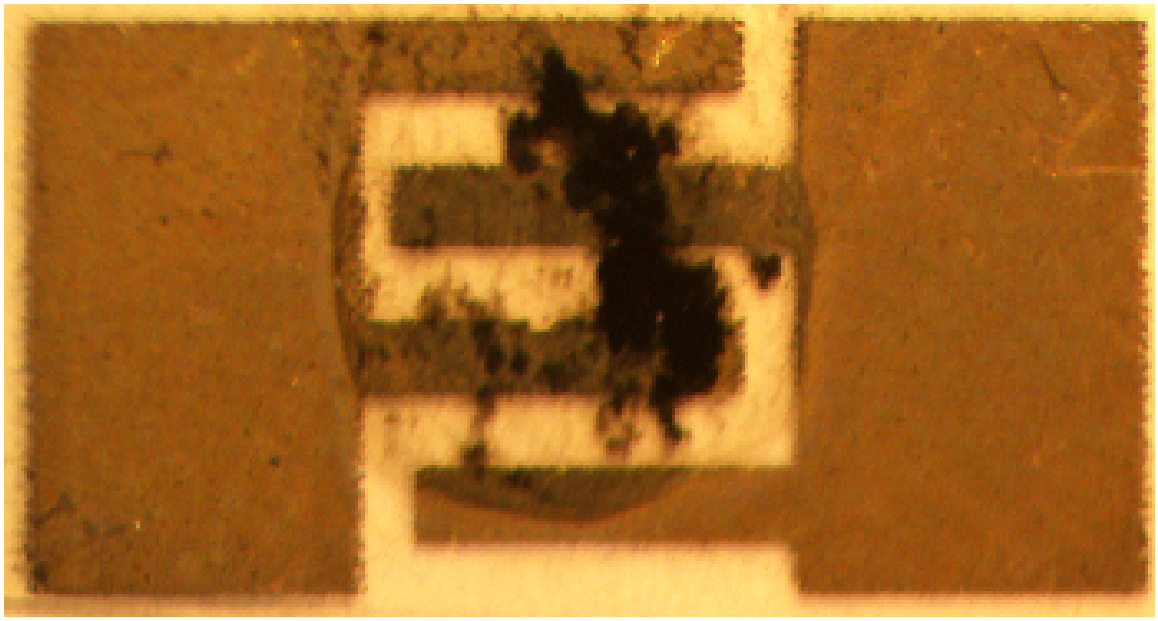

Figure 4.2. Complete BNNT and MWCNT sensor (NPS4). The deposit on this sensor is darker than the one in figure 4.1 due to 7.5 µL being used for this sensor

4.2 Resistance After Exposure

The reported resistances in Table 4.1 prior to exposure were measured with the Arduino board since during the exposure the resistances would be monitored with the board as well. Since the mechanism for changing the resistance was theorized as the thermal neutron flux interacting with the BNNTs, obtaining a close estimate of the area of the BNNT and MWCNT deposit was necessary in order to calculate the total number of neutrons that the sensor was exposed to. Table 4.2 lists the BNNT/MWCNT deposit area, the total number of neutrons that the sensor was exposed to, and the final resistance. The total exposure (number of neutrons) was calculated using

$$Number\ of\ Neutrons = \frac{S}{4\pi d^2}\ x\ Exposure\ Time\ x\ Deposit\ Area \tag{4.1}$$

where S is the source strength and d is distance from the source. The source strength is already accounting for the poly shielding used to moderate the incoming neutrons. Figure

4.3 shows the area measured to calculate the deposit area.

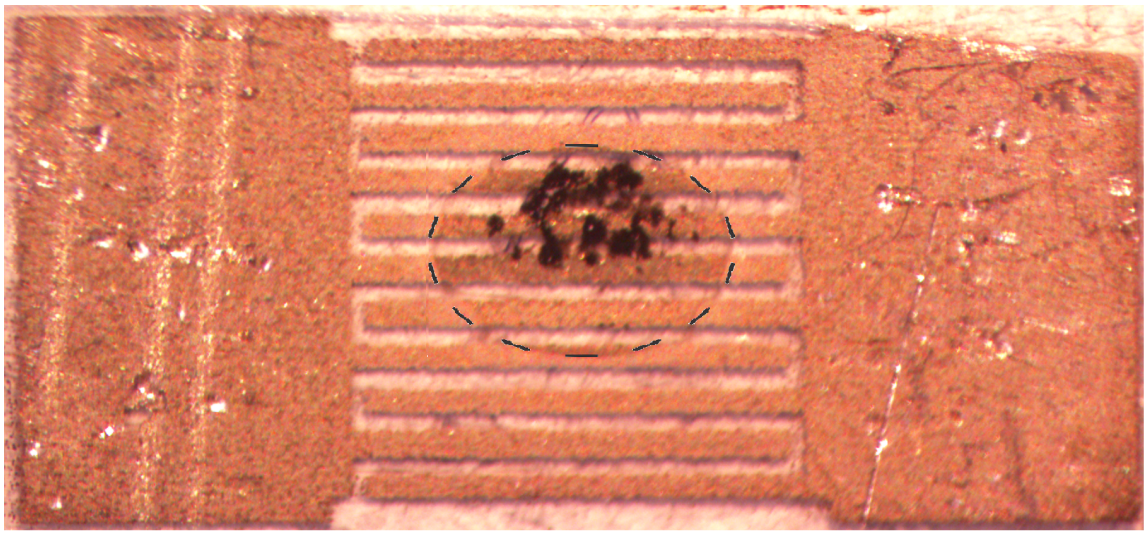

Figure 4.3. Picture of resistor NPS2 showing the area marked by the black oval as the area measured to calculate the deposit area of the BNNT/MWCNT mixture. The deposit area is 0.87 mm^2.

Table 4.2. List of final resistances with deposit area and the total sensor exposure

Resistor	Deposit Area (mm^2)	Number of Neutrons	Final Resistance (kΩ)
NASA1	0.63	230	72.1
NASA2	0.71	42006	2.15
NASA3	0.21	2580	1.79
NPS1	1.71	654804	9.89
NPS2	0.87	13200	2.83
NPS3	3.65	72417	50.2
NPS4	2.55	15315	10.6
NPS5	4.25	18271	660

Based on the microscopic cross section of boron being 3840 barns, an example deposit area of 0.5 mm^2, a deposit thickness of 10 microns, the concentration of boron in the deposited

solution being 5 x 10^{-4}g/mL, and the molecular mass of boron, roughly 44% of the incident neutrons will cause the (n,α) reaction. This was calculated using

$$\Sigma = n\sigma \tag{4.2}$$

where Σ is the macroscopic cross section for neutron absorption, n is the concentration of Boron-10 in the deposited solution, and σ is the microscopic cross section of Boron-10 (3840 barns). Then to find the probability of a neutron interacting with Boron-10 is simply

$$Probability = 1 - e^{-\Sigma x} \tag{4.3}$$

where x is the distance traveled by a neutron through the material (estimated as 10 microns). This is a rough estimate since each deposit area is different which would mean that the thickness of each deposit would be different, changing x for each calculation.

The number of neutrons that each sensor was exposed to varies for a few reasons. One reason being that each deposit area was different. Also, the length of time each sensor was exposed to neutron radiation varied slightly between each exposure. Lastly, the energy spectra of the thermalized neutron sources that each detector sample was exposed to were different. So length of exposure and the sources that each resistor were exposed to varies the number of neutrons that reach the sensor.

With the final resistance measured, the initial and final resistances were compared in order to calculate a percent change. A higher percent change means that a larger percentage of the nanotube connections across the interdigitated electrodes have been broken during the exposure. An opening assumption was that if there are too few percolative connections (high initial resistance), the high-energy α particle or Li-7 product from the (n,α) reaction would have a low probability of breaking one of those connections (the number of targets is small, thus the probability of hitting a target is small). On the other hand, with too many connections (low initial resistance), even if the high energy α does break a connection, the resistance will not change dramatically, since the percentage change in connections will be low. That indicates that the percent change of resistance for a given neutron flux (detector

sensitivity) will be lower on both the low and high end of the resistance span. Table 4.3 shows initial and final resistances for each resistor as well as percent change. Figure 4.4 shows percent change in resistance based on initial resistance. Figure 4.5 shows the same data with the data from Hameed and Gats [7] included.

Table 4.3. List of percent change from initial to final resistance

Resistor	Initial Resistance (kΩ)	Final Resistance (kΩ)	Percent Change in Resistance (%)
NASA1	59.75	72.1	17.2
NASA2	1.582	2.15	26.3
NASA3	1.634	1.79	24.1
NPS1	6.94	9.89	29.8
NPS2	2.45	2.83	13.6
NPS3	45.84	50.2	8.69
NPS4	10.14	10.6	4.61
NPS5	638	660	3.36

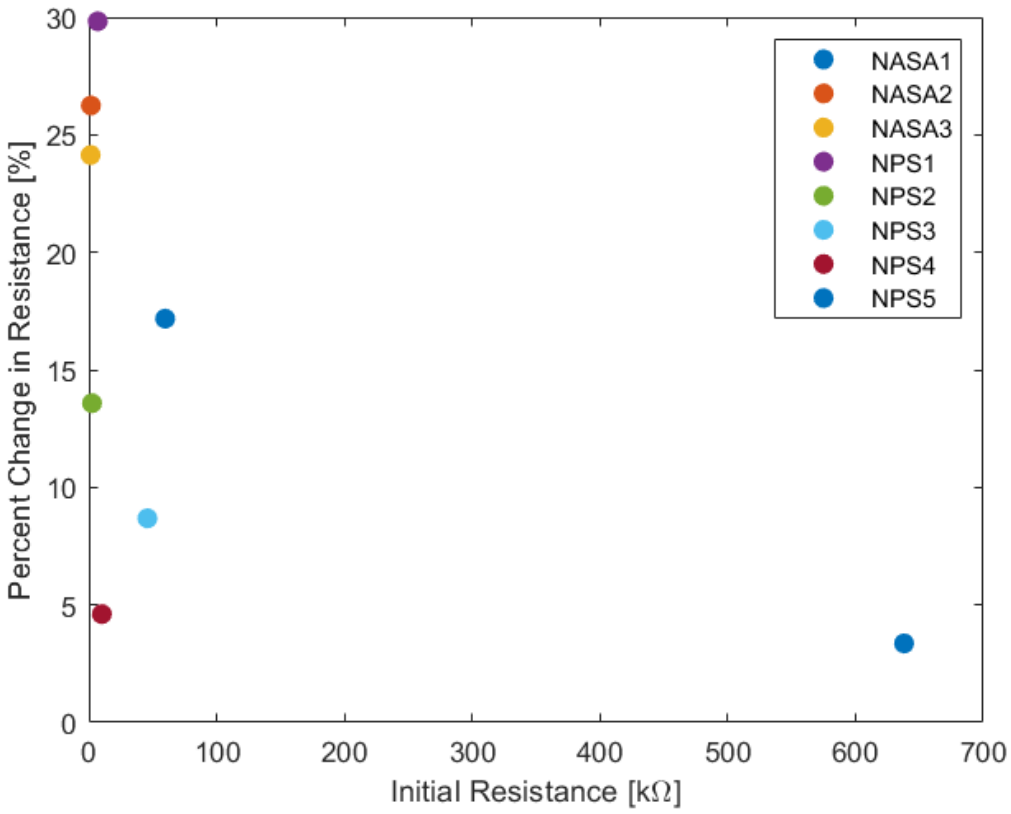

Figure 4.4. Percent change in resistance vs. initial resistance for data collected during this thesis

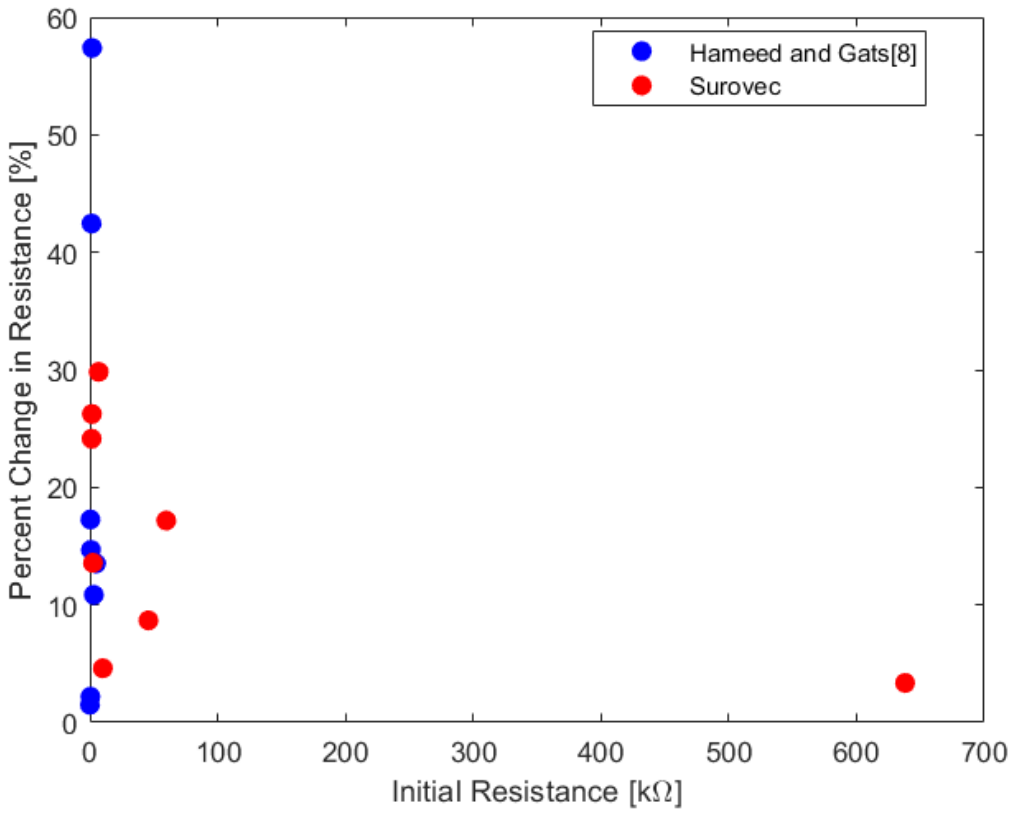

Figure 4.5. Percent change in resistance vs. initial resistance for data collected for this thesis and the data from Hameed and Gats. Source: [7].

The data from this thesis and the data from Hameed and Gats show a trend of the percent change in resistance increasing with increase in resistance until roughly 2.5 kΩ and begins to fall after that. Figure 4.6 shows this trend more clearly with zooming in on the data from 0 kΩ to 15 kΩ. The initial resistances that yielded the highest percent changes in resistance after exposure are those in the range of roughly 2 - 2.5 kΩ with lower and higher initial values experiencing lower percent changes (especially visible in Figure 4.5).

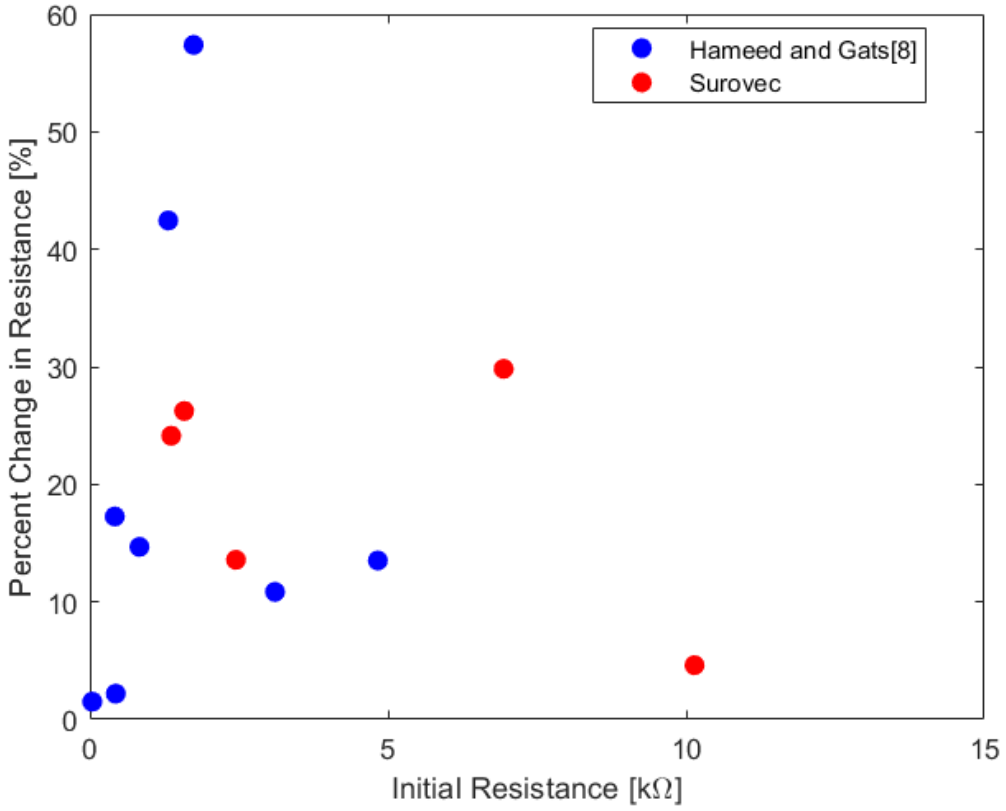

Figure 4.6. Percent change in resistance vs. initial resistance with only the data with an initial resistance from 0 - 15 kΩ. The trend of the percent change increasing until roughly 2.5 kΩ then decreasing is visible

4.2.1 Exposure Results

Again, the hypothesized mechanism for these sensors changing resistance is the breaking of CNT bridges across the interdigitated finger electrodes of the resistor. If there are too many nanotube connections, breaking one connection will not have a large effect on the overall resistance of the sensor. On the other hand, if the number of connections is too small, the α's from the (n,α) reaction in the Boron-10 will have a smaller chance of interacting with one of the CNT bridges. If the α particles have too small a probability to break the CNT bridges, then the resistance will not change for a given exposure. Therefore, the conclusion to be drawn, that seems to be confirmed by the data in Figures 4.5 and 4.6, is that there

exists an ideal range of initial resistances that provides enough CNT connections that the α particles have a high enough probability to break a connection, but not too many, so that breaking a single connection will have no appreciable effect on the overall resistance of the sensor. Figure 3.3 showed a drawing of the idea related above. In the bridge labeled 1, breaking one of the nanotubes will break that connection, but if you only have a few of these connections there will be a very low chance of the α reaching and breaking the CNT. However in the second example, if one of the CNTs are broken, this will not appreciably change the resistance of the entire set of connections.

Another important observation is that when a single nanotube is broken in (1) in Figure 3.3, that entire pathway is removed from the overall conductance/resistance value. No matter how many more CNTs are broken on this same connection, the overall resistance will not change. This implies that these sensors can be saturated to the point that exposing the sensor to more neutrons will not break a noticeable number of connections, producing no additional change in resistance. The assumption of saturation has been verified experimentally in both our measurements and Hameed and Gats [7]. Therefore, some balance must exist between having too many nanotubes and too few nanotubes making the connections. Lastly, supporting the calculations of the number of connections across the interdigitated electrodes, (3) in Figure 3.3 shows that even if there are CNTs arranged in this orientation, it is equivalent to having two separate connections and the equivalent resistance can be calculated as two resistors in parallel.

As table 4.2 shows, the number of neutrons each sensor was exposed to varies. While this could lead to a larger or smaller change in resistance after exposure, how the neutrons are affecting the resistance must be considered. First, using equation 3.2, the number of CNT connections severed can be calculated by comparing the initial and final resistances. Table 4.4 shows the estimated initial number of connections for each sensor based on the 200 Ω/μm resistance of a single MWCNT [20]. The numbers for the CNT connections were calculated using Equation 3.3 and using the initial resistances. Figure 4.7 shows how increasing the number of connections decreases the initial resistance.

Table 4.4. List of the CNT connections for each resistor

Resistor	Initial CNT Connections	Final CNT Connections	Change in CNT Connections	Percent Change in CNT Connections (%)
NASA1	1.51	1.25	0.259	17.2
NASA2	56.9	54.7	2.18	3.83
NASA3	66	64.4	1.6	2.43
NPS1	1.3	9.10	3.87	29.8
NPS2	36.7	31.7	4.99	13.6
NPS3	1.96	1.79	0.171	8.69
NPS4	17.8	16.9	0.818	4.61
NPS5	0.282	0.273	0.009	3.36

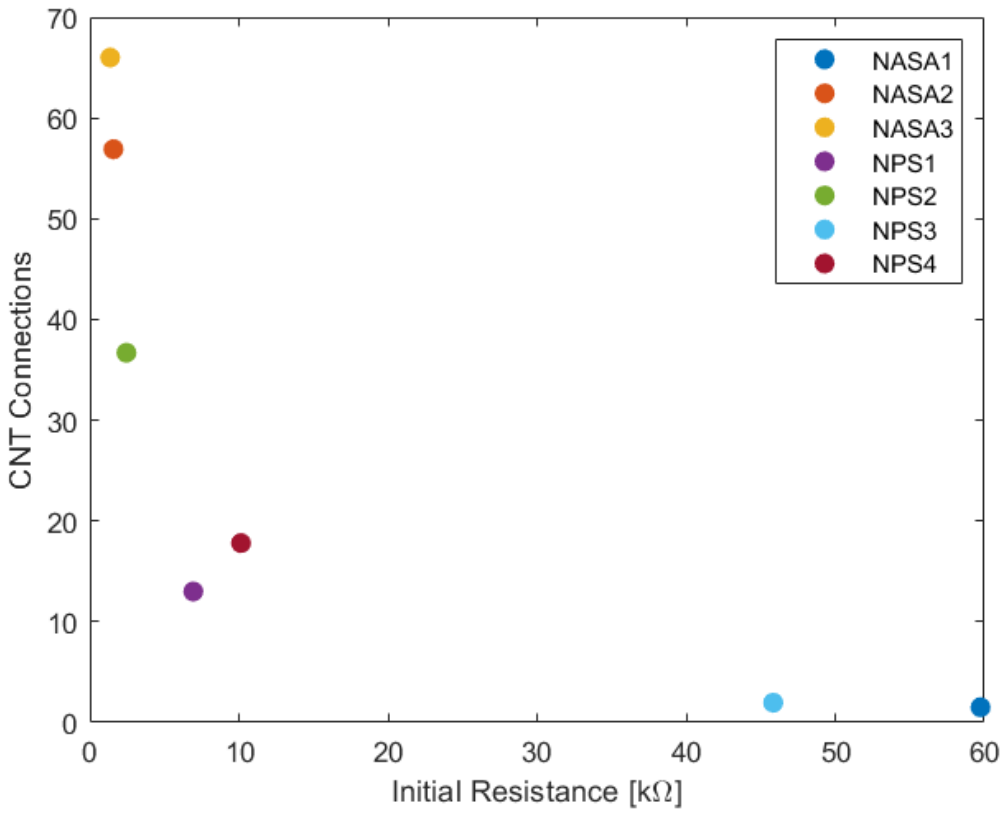

Figure 4.7. Initial number of CNT connections across the interdigitated electrodes vs. initial resistance of the sensor

We also consider the relation between number of neutrons required to break a CNT conductive pathway to initial resistance zoomed in on the area of interest as selected for the Figure 4.6. This is shown in Figure 4.8. The number of neutrons per connection broken was calculated by taking the total number of neutrons the sensor was exposed to, from table 4.2, and dividing that by the change in the number of CNT connections from Table 4.4 for each detector. A clear increase in the number of neutrons per connection broken with an increase in resistance is visible. This supports the claim that with increasing resistance, there is a smaller probability of the α interacting with the CNT connection across the interdigitated electrodes. With a larger resistance, there are fewer connections, making each connection a smaller target and requiring a larger number of neutrons to sever a connection.

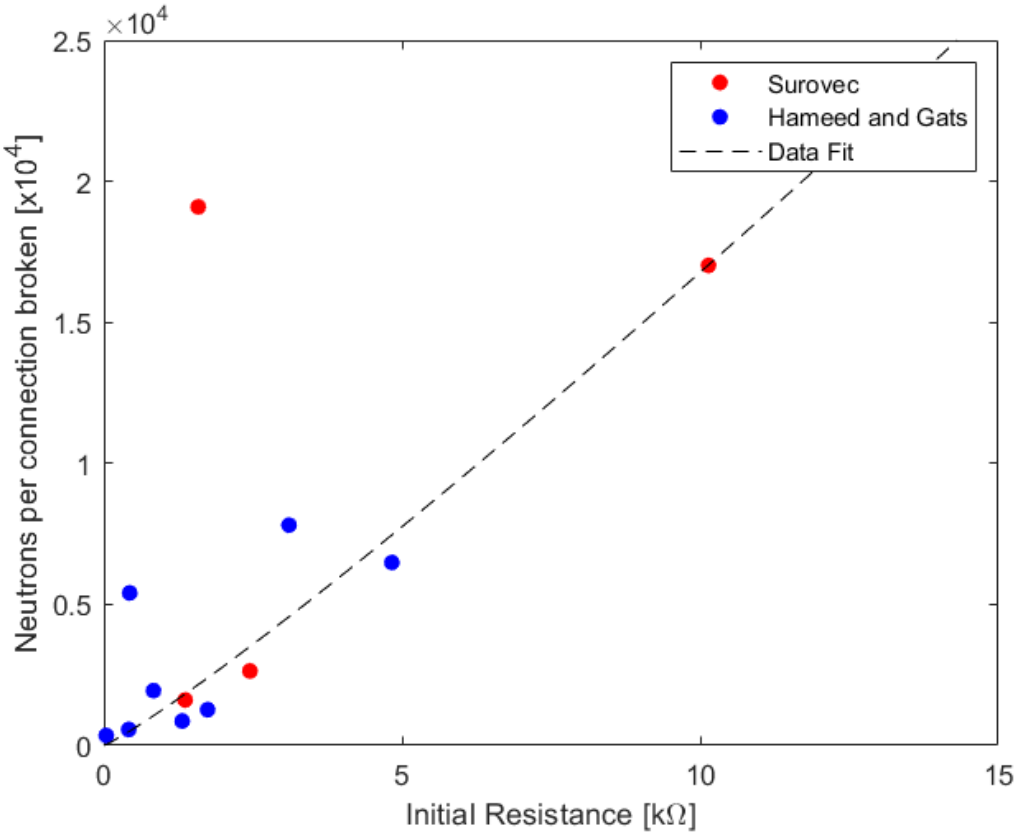

Figure 4.8. Number of neutrons required to break a CNT connection vs. initial resistance

The highest red data point (resistor NASA 2) was discarded for the fit line. This sensor is theorized to be over-exposed. If a connection is completely severed so that there is no path for current to flow, exposing the sensor to more neutrons will not change the resistance. So some saturation point exists that the sensor will begin to plateau since the CNT connections have mostly been severed. The BNNT to CNT connection ratio has decreased enough that the additional neutron exposure does not have a high enough probability to sever a CNT connection with an α particle.

4.2.1.1 Ideal Range for Initial Resistance

Data in Figure 4.7 represents the number of connections for any given initial resistance and is given by Equation 3.2. However, due to different electrode configurations for different

sensors, a power-law fit needed to be done on data in Figure 4.7. To get the fractional change in resistance for a single broken connection, we divide 1 connection by the total number of connections. This is simply the inverse of Equation 3.3 which gives us

$$\frac{1}{n} = \frac{R_{eq}}{R} \tag{4.4}$$

again where R_{eq} is the initial resistance and R is the resistance of a single CNT connection. As the initial resistance increases, the 1/n value (the fractional change in CNT connections per broken CNT connection) will increase linearly. Due to differences in electrode separation lengths, the inverse fit of Figure 4.7 needed to be taken. The equation resulting from this fit is

$$\frac{Fractional\ Change\ in\ CNT\ Connections}{Broken\ Connections} = \frac{1}{n} = \frac{R_{eq}^{0.993}}{89.9} \tag{4.5}$$

where n is the initial number of connections. The exponent for initial resistance of 0.993 in Equation 4.5 is expected to be 1 as predicted by Equation 4.4. Since 0.993 is close to 1, moving forward Equation 4.6 is used.

$$\frac{1}{n} = \frac{R_{eq}}{89.9} \tag{4.6}$$

Data in Figure 4.8 represents the number of neutrons needed to break a connection. This data has an exponential fit. Inverting the data will give us Figure 4.9 which is number of broken connections per a single neutron as a function of initial resistance.

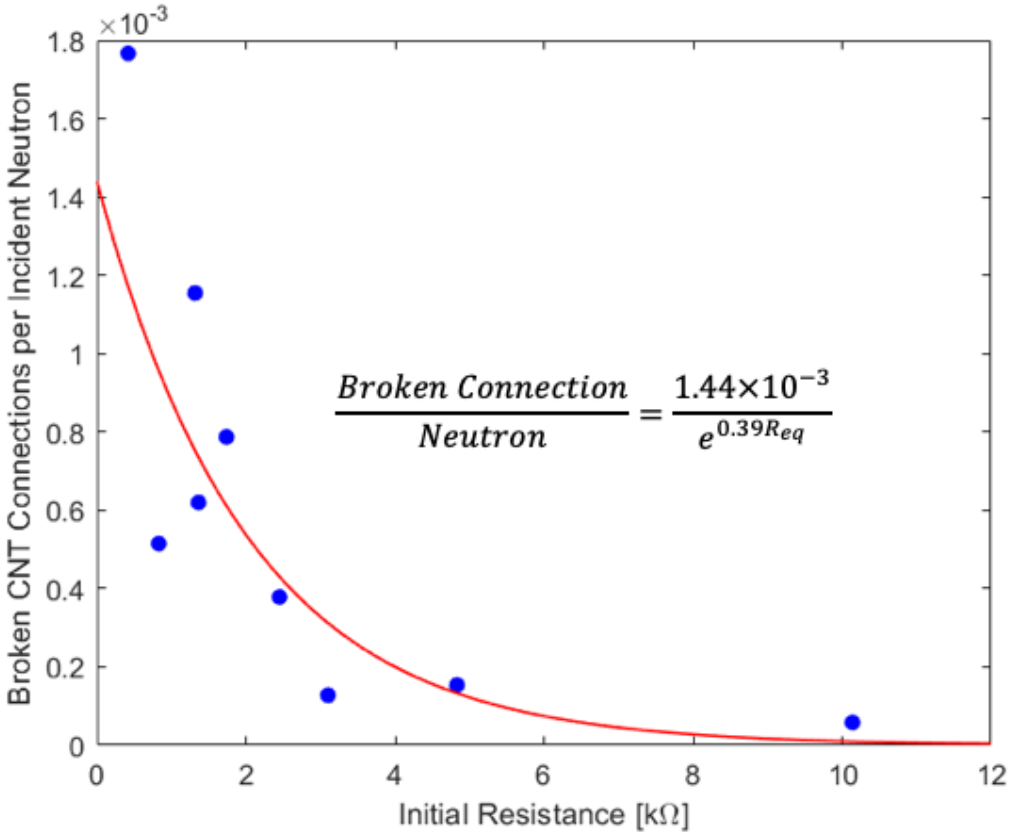

Figure 4.9. Broken CNT connections per incident neutron vs. initial resistance. The lower initial resistance, the more connections are available for neutron interaction (larger target), therefore it should take fewer incident neutrons to break a CNT connection.

The fit of this data is

$$\frac{Broken\ Connections}{Neutron} = \frac{1.44x10^{-3}}{e^{0.393R_{eq}}} \tag{4.7}$$

Equation 4.6 and 4.7 are plotted in Figure 4.10 showing how the first is linearly increasing, and the latter is exponentially decreasing. Then multiplying Equation 4.6 and 4.7 allows the cancellation of broken connections in the numerator of Equation 4.6 with the denominator of Equation 4.7 which results in

$$\frac{Fractional\ Change\ in\ CNT\ Connections}{Broken\ Connections} x \frac{Broken\ Connections}{Neutron} = \frac{Fractional\ Change\ in\ CNT\ Connections}{Neutron} \tag{4.8}$$

The resulting equation then becomes

$$\frac{Fractional\ Change\ in\ CNT\ Connections}{Neutron} = \frac{1.6x10^{-5}R_{eq}}{e^{0.393R_{eq}}} \tag{4.9}$$

which is plotted as the red line in Figure 4.11 which also includes the experimental data for each resistor in the 0 - 10 Ω range from Hameed and Gats [7] and this thesis.

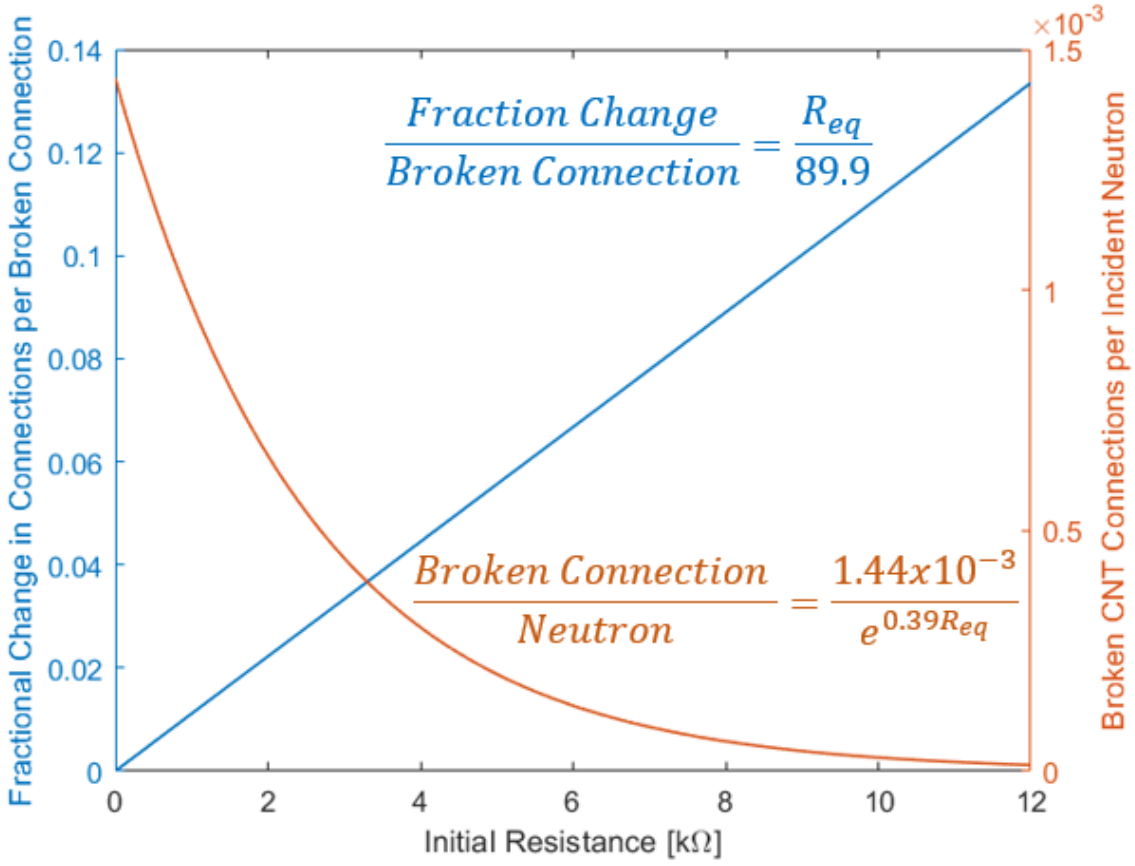

Figure 4.10. Fractional change in connections per broken CNT connection and broken CNT connection per incident neutron vs. initial resistance

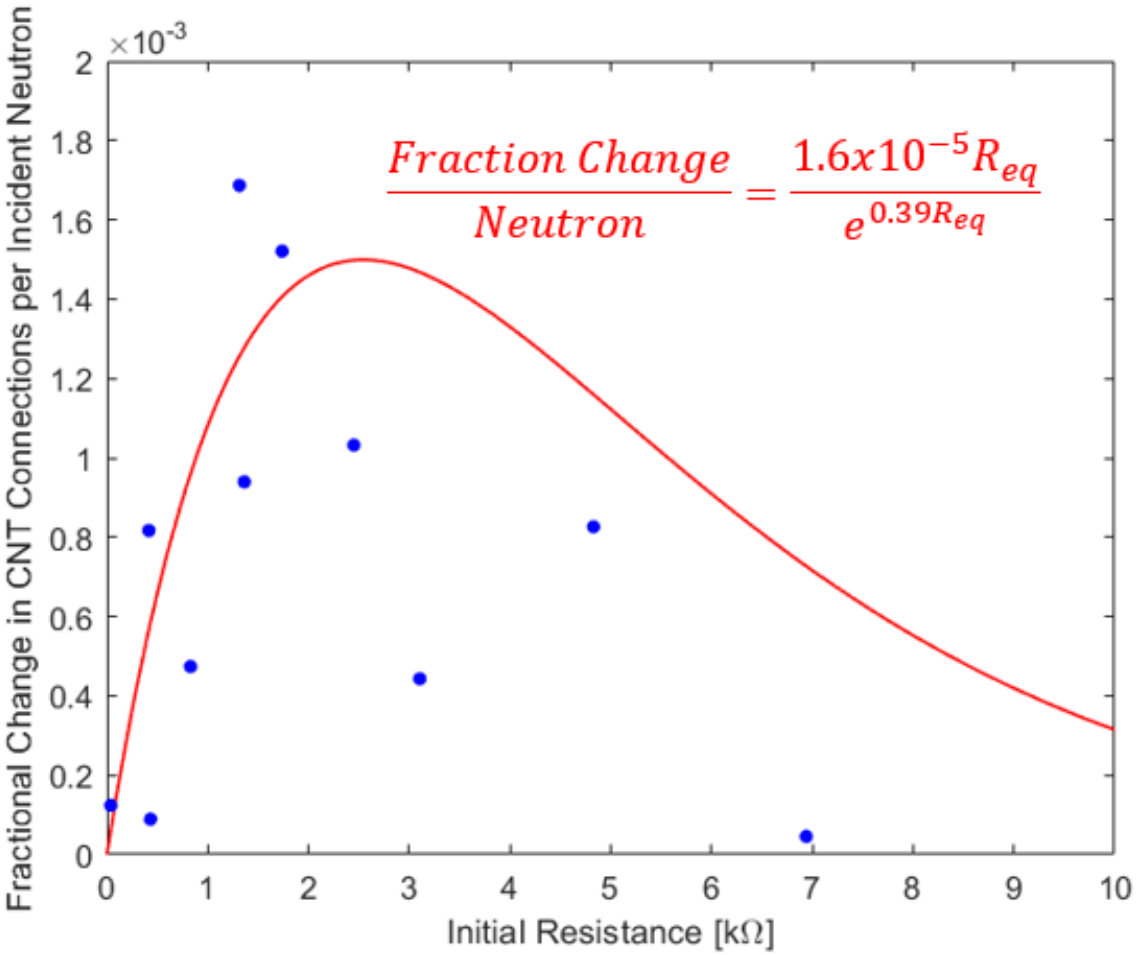

Figure 4.11. Fractional change in CNT connections per incident neutron vs. initial resistance including data from Hameed and Gats. Adapted: [7].

The behavior of the plots in Figures 4.10 and 4.11 reinforce the earlier assumptions that at the low resistances, there are many connection pathways to break (orange plot) but their breakage yields a small fractional change in connections (blue plot) yielding small overall sensitivity. On the other hand, high resistances, stemming from a few number of connections to break (orange plot), make each breakage a larger fractional change in connections (blue plot). However since there are few connections, this is a smaller effective target again yielding a small overall sensitivity. Therefore, based on the data collected for this thesis and Hameed and Gats [7], the conclusion that some ideal initial resistance range exists that would produce the most sensitive resistor to incident neutrons is supported. It does

seem the range between 2 and 4 kΩ would produce the largest fractional change in CNT connections per incident neutron (largest change in resistance). Since fractional change in CNT connections per neutron is directly proportional to the resistance change for any given exposure, we can say that the trend in Figure 4.11 explains the trend in percent change in resistance vs. initial resistance (or detector sensitivity) displayed in Figure 4.6.

4.3 Dependence of Resistance on Voltage

The Arduino board provides a 5 VDC potential to measure the resistance in the circuit shown in figure 3.6. A standard multimeter typically uses 1.5 V potential for resistance measurement. This difference in voltage for measuring the resistance of the sensor directly affected the measured resistance. With the increase in voltage, the current through the resistor increased, theoretically heating up the resistor. With this increase in heat resulting from the increase in voltage, a decrease in resistance was noticed when measuring the resistance with the Arduino board vice the multimeter. To verify this, the sensors were placed in a parametric analyzer and a 5 V sweep was performed while measuring the current across the resistor. Using Ohm's Law ($V = IR$), the resistance can then be calculated concurrently. Figure 4.12 shows how increasing the voltage decreases the resistance for sensor NASA 1, indicating that the increase in current is resulting in a slight increase in temperature. The remaining resistors are presented in Appendix A.1.

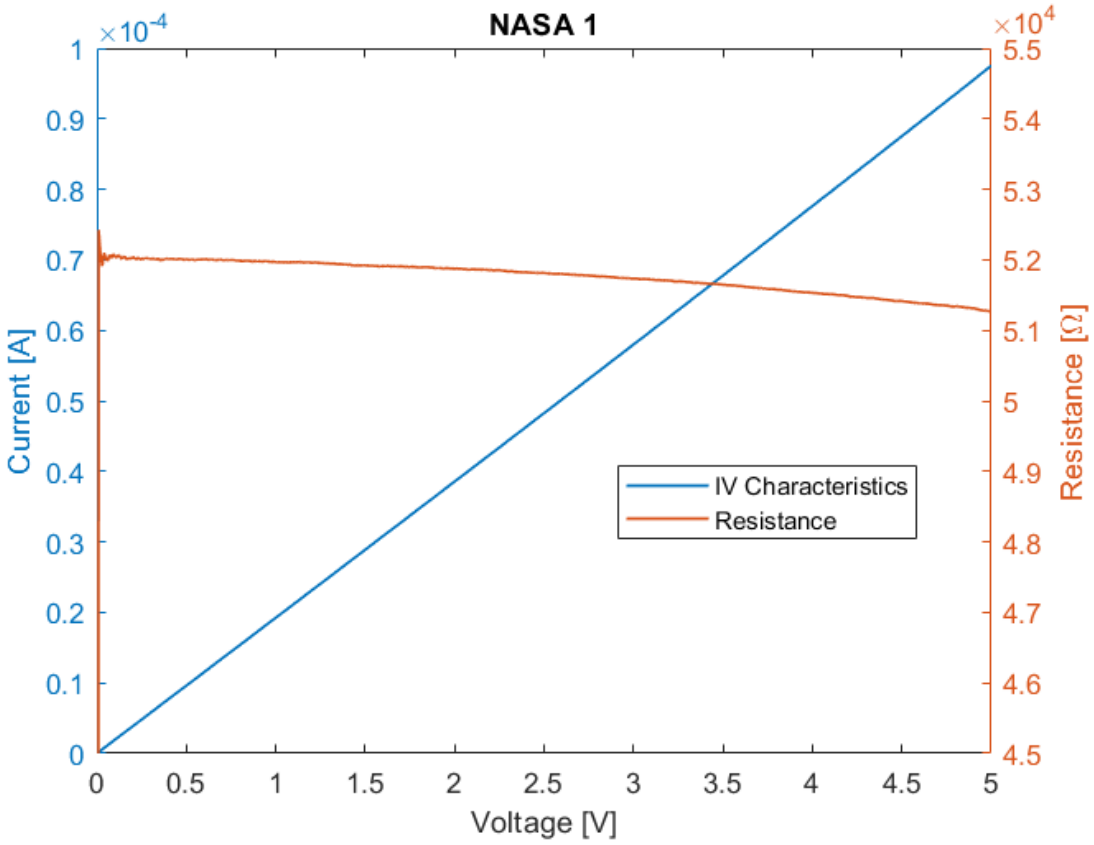

Figure 4.12. Current and Resistance vs. voltage for resistor NASA 1. The slight drop in resistance with increasing voltage is clearly visible

Additionally, during the exposure of the sensor to neutrons, the resistance experienced unexpected drops. Once the exposure was stopped and the sensor was measured after a few days, the resistance did increase as expected implying that CNT connections were severed. However, during the exposure, the resistance was not gradually increasing, instead the resistance decreased. As shown in Equation 2.1 and 2.2, 2.79 MeV of energy is released during the reaction of the thermal neutrons with the boron-10. This energy is hypothesized to be causing a slight increase in temperature of the MWCNTs on the sensor, which would explain the slight decrease in resistance. Figure 4.13 shows the trend of resistor NPS1 during exposure. Thermal effects of the reaction, combined with the effects of reading out with 5V source, probably overwhelmed the effects of severing the percolative conductive pathways. This resulted in observed overall reduction of resistance during exposure.

This effect made it difficult to use the Arduino for continuous monitoring and we had to focus on the initial and final values. Follow-on work needs to be done where the Arduino voltage is reduced to 1.5 V or lower.

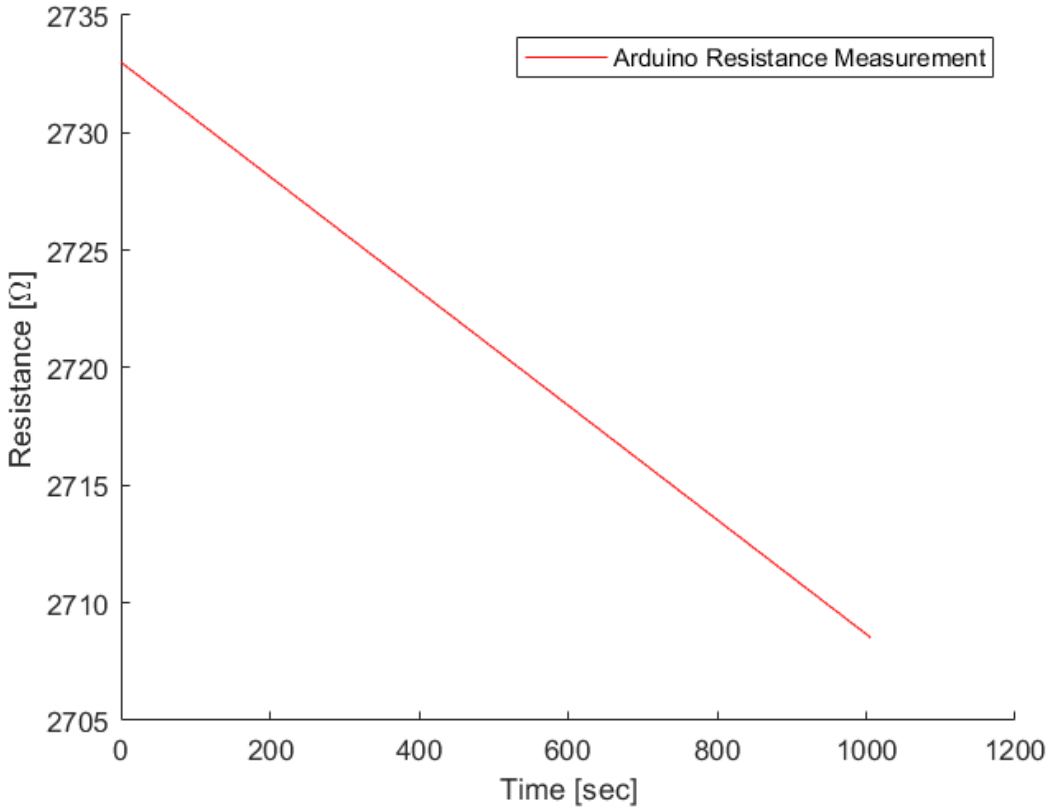

Figure 4.13. Resistance vs. time during the exposure of NPS1 to the Cf-252 source

CHAPTER 5: Conclusion

The current research aimed at finding ideal concentrations of BNNTs and MWCNTs to yield the largest percent change in resistance when the MEMS sensors were exposed to neutron radiation. By including the data from Hameed and Gats experimentation [7], and performing additional testing on sensors built for this thesis, a hypothesized ideal initial resistance was discovered. Using these results, additional work can be done to develop improved processes to fabricate sensors designed for optimal sensitivity.

5.1 Conclusion for MWCNT and BNNT MEMS Neutron Sensor

The results from this project confirmed the conclusions of Hameed and Gats as well as added valuable data. The goal of the thesis was to attempt to find an ideal initial resistance of the MEMS sensor in order to provide the maximum percentage change in resistance from neutron exposure. Using the boron-10 and MWCNT mixture deposited on the interdigitated electrode, a clear region between 2 and roughly 4 kΩ exists that yields the maximum percent change in resistance.

Additionally, aside from the main research objective, the temperature dependence of the resistive sensors was discovered to be aligned with the changing resistance of CNTs as described by Harris [20]. The resistance was verified to decrease with increasing temperature by running the sensors through a 5 VDC sweep using a parametric analyzer. With this, as well as the susceptibility of the sensor to light described by Hameed and Gats [7], knowing the operating environment of the sensor is a requirement for the accuracy of the sensor. If calibrated properly, the resistance change due to thermal effects could be removed from the final output signal. This would allow continual measurements of neutron exposure levels.

The mechanism for changing the resistance was verified throughout the experimentation of this thesis. Also, the fact that the BNNT to MWCNT connection ratio determined the number of neutrons required to break a connection was discovered. A hypothesis that an ideal ratio existed was confirmed (Figure 4.11). In simple terms, both low and high

resistances exhibit lower sensitivities. Low resistance detectors have a large number of connections and even though they need fewer neutrons to break a connection, each breakage creates a small fractional change in overall resistance. The combination of those two effects leads to low overall sensitivity. Broken connections in the high resistance detectors, on the other hand, create large fractional changes in resistance, but they are a "smaller target" and require many more neutrons to be broken. Again, the combination of these two effects creates low overall sensitivity. The points are illustrated in Figure 4.10 and 4.11.

5.2 Recommendation for Continued Work

Throughout the course of design and experimentation, many areas of improvement were identified. The mixing process of the MWCNTs and BNNTs can be improved to offer a more uniform dispersion of the solution. While much research was completed to properly mix the MWCNTs, BNNTs are a newer area of study and less data exists on their suspension in water. One possible improvement could be the use of a surfactant during the process of sonicating the BNNTs in water. Surfactants are commonly used for better mixing of materials that are either hydrophobic or difficult to mix with water due to density differences. The BNNTs did begin to aggregate with time in solution possibly causing inconsistent amounts of the mixture to be deposited on the printed electrode, despite the physical amount drawn into the pipette to be the same.

The conclusions drawn on the ideal range of initial resistance need to be reinforced with more data. More sensors need to be fabricated to fill in the gaps in the trend of percent change in resistance after exposure vs. initial resistance. However, in order to do more testing of the fabricated sensors, the deposition process must be improved to have a more predictable way of ensuring a consistent initial resistance with some amount of solution deposited. Additionally, a more consistent size of the deposited nanotubes would be ideal to ensure the exposures were similar. For this thesis, the neutron exposure varied widely due to the different size of each nanotube bundle on the sensor. In order to further verify the result of how much exposure is required to break a CNT connection based on the initial resistance, the exposure must be held constant. Although this thesis did design some sensors that had different geometries, the results were not conclusive if the sensors with larger gaps between the interdigitated fingers reacted any differently to the neutron exposure.

Lastly, the accurate real time measurement of the resistance of the sensor can be improved. The Arduino board operated at a high enough voltage that the potential seemed to be heating up the sensor and influencing the resistance of the sensor. The resistance would increase after the exposure was stopped and the resistor was allowed to rest for some time. The design of a circuit that can measure the resistance while applying a lower voltage could allow the change in resistance to be monitored in real time, providing valuable data to verifying the results of this thesis.

THIS PAGE INTENTIONALLY LEFT BLANK

APPENDIX A:
IV Characteristics

The IV characteristics for resistor NASA1 are shown in Chapter 4 in figure 4.12. The remaining resistors IV characteristics are contained in this appendix.

A.1 Graphs of IV Characteristics

Below are plots of the IV characteristics of all resistors.

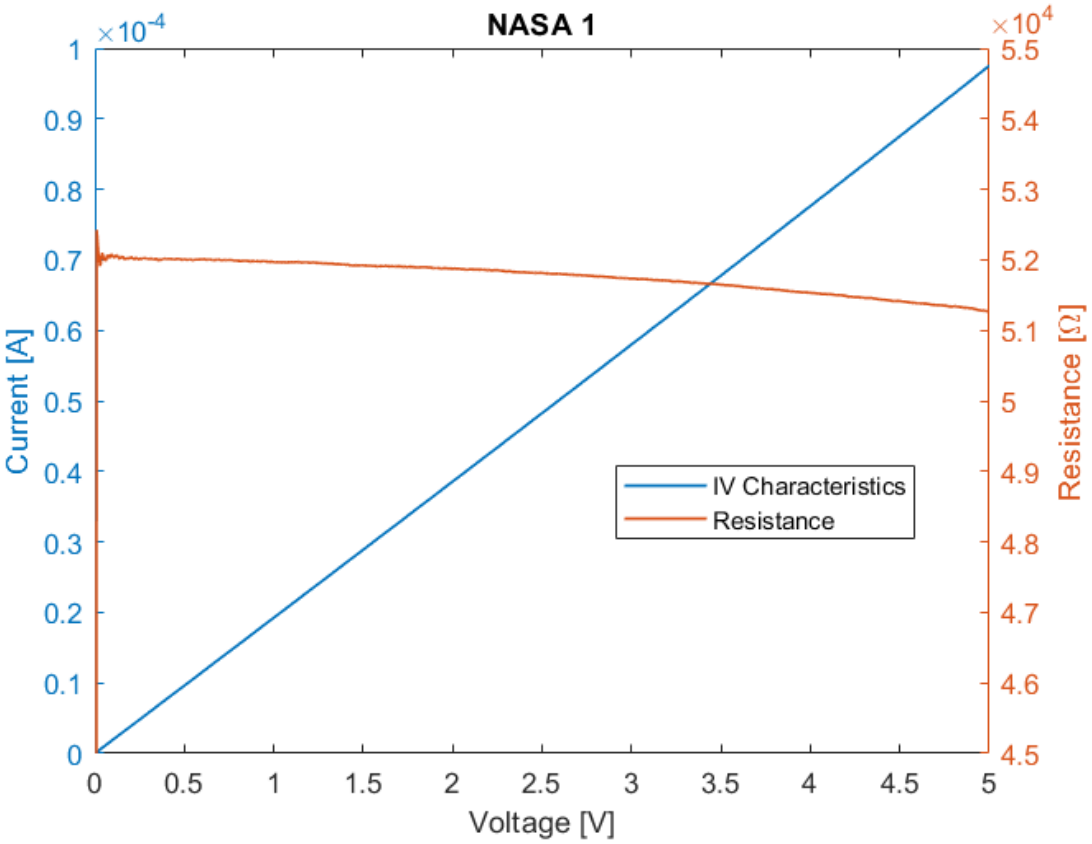

Figure A.1. NASA1 IV characteristics and the dependence of resistance on voltage as measured by a parametric analyzer

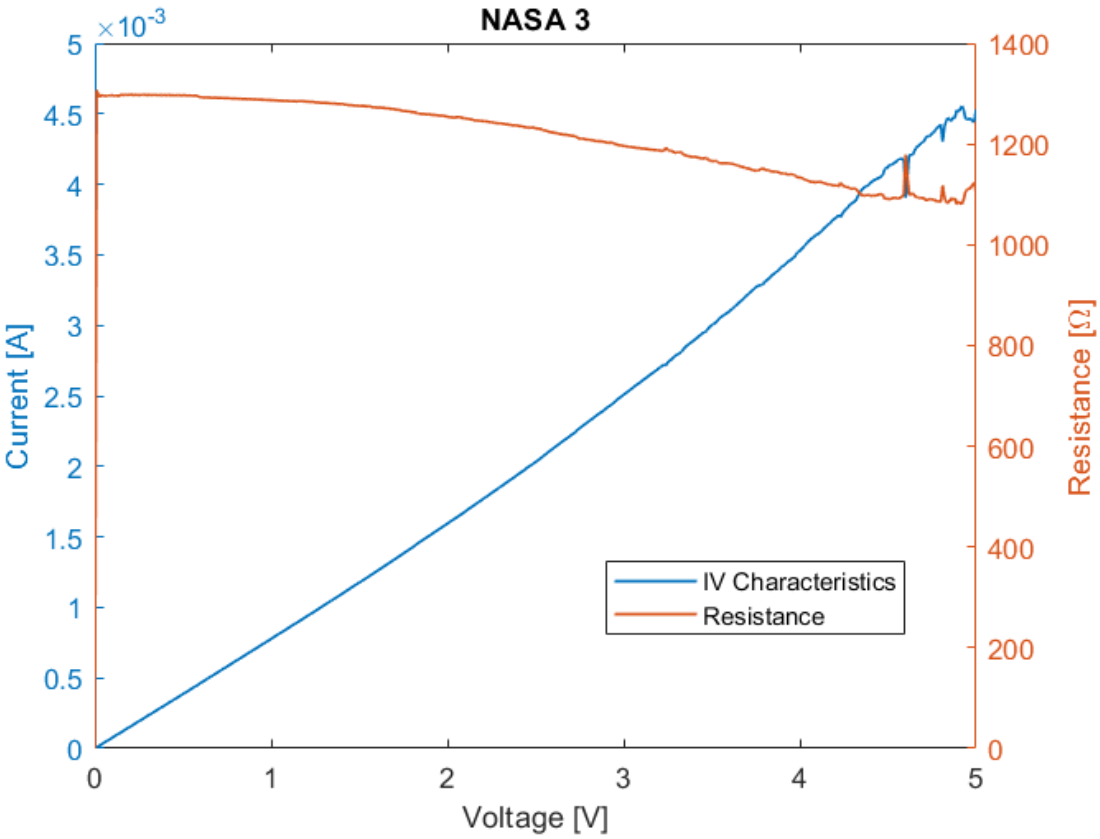

Figure A.2. NASA3 IV characteristics and the dependence of resistance on voltage as measured by a parametric analyzer

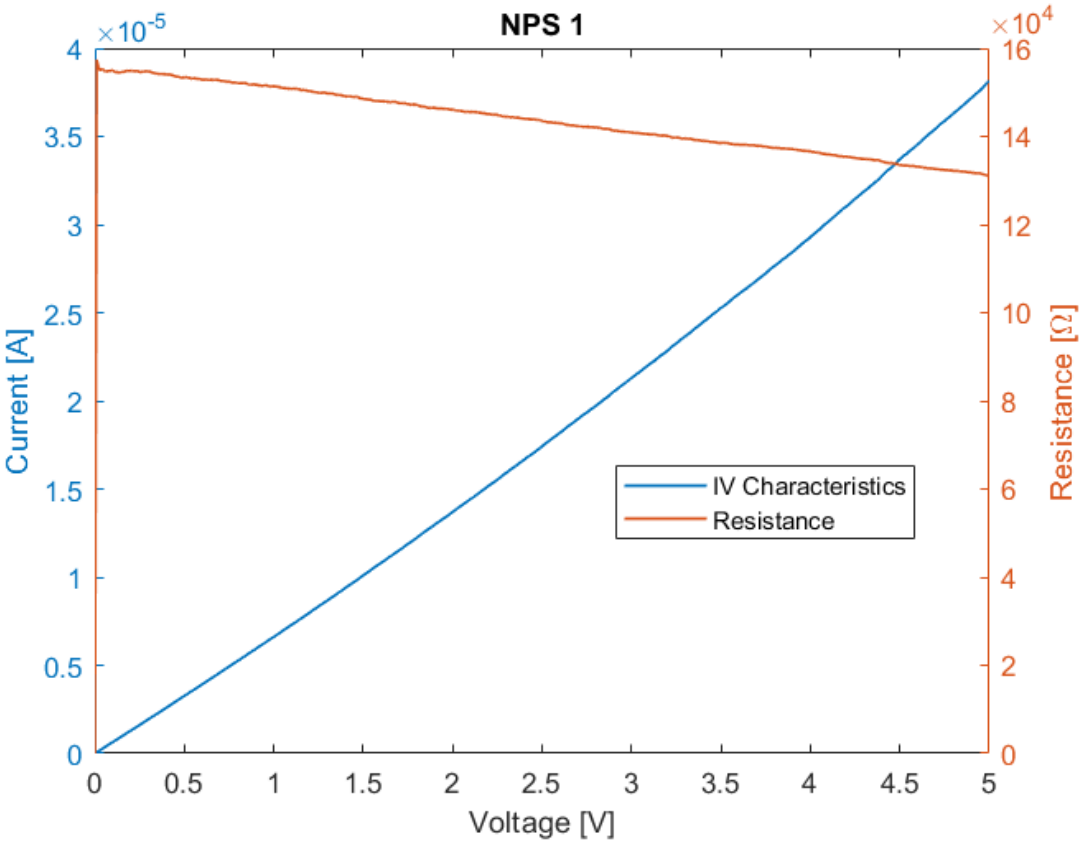

Figure A.3. NPS1 IV characteristics and the dependence of resistance on voltage as measured by a parametric analyzer

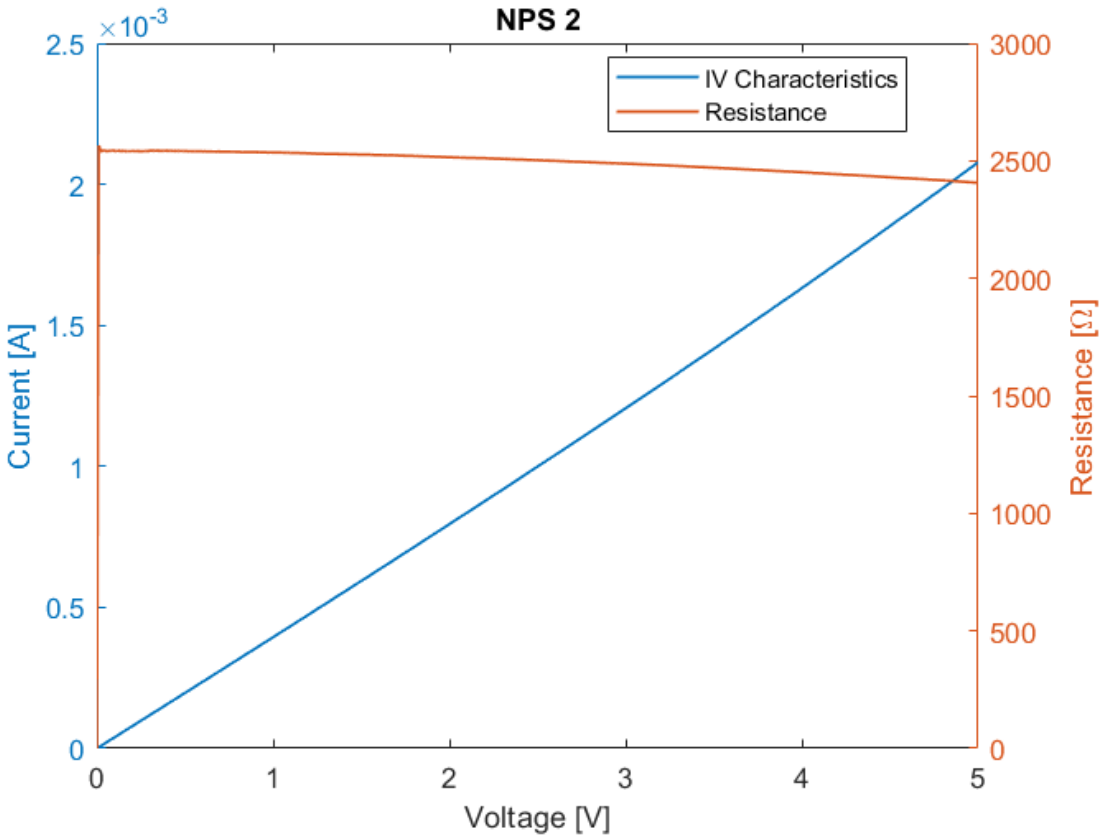

Figure A.4. NPS2 IV characteristics and the dependence of resistance on voltage as measured by a parametric analyzer

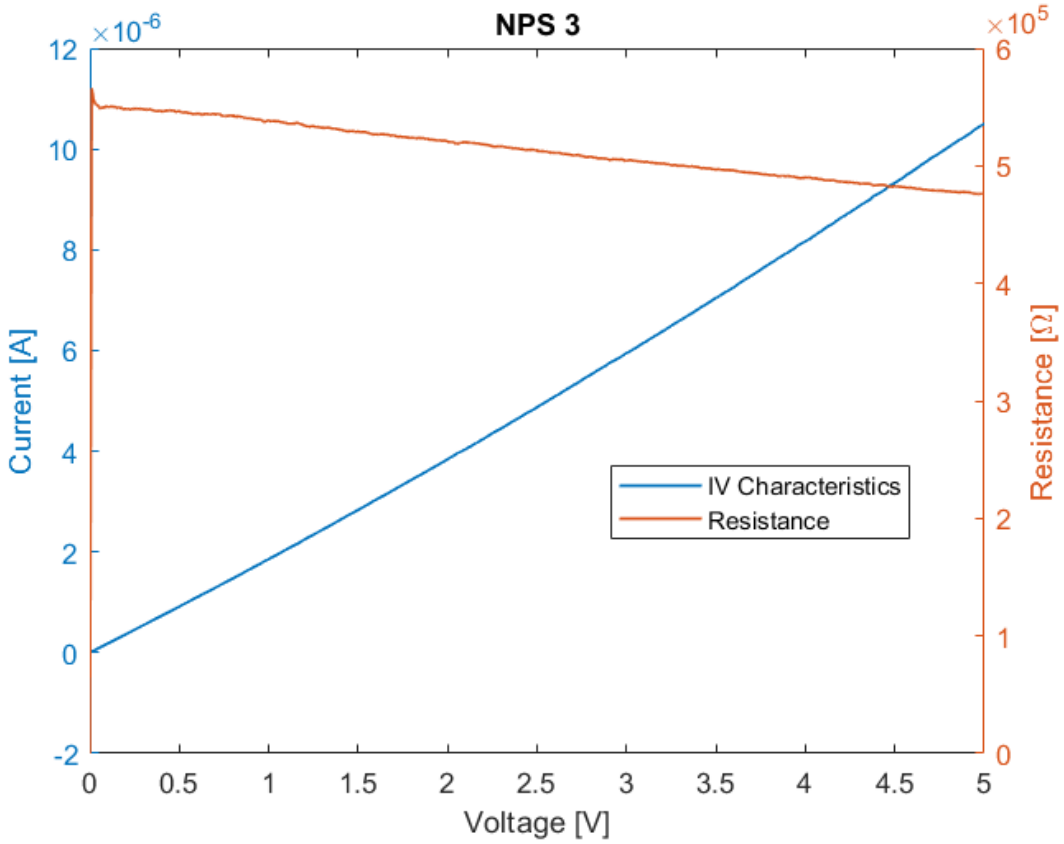

Figure A.5. NPS3 IV characteristics and the dependence of resistance on voltage as measured by a parametric analyzer

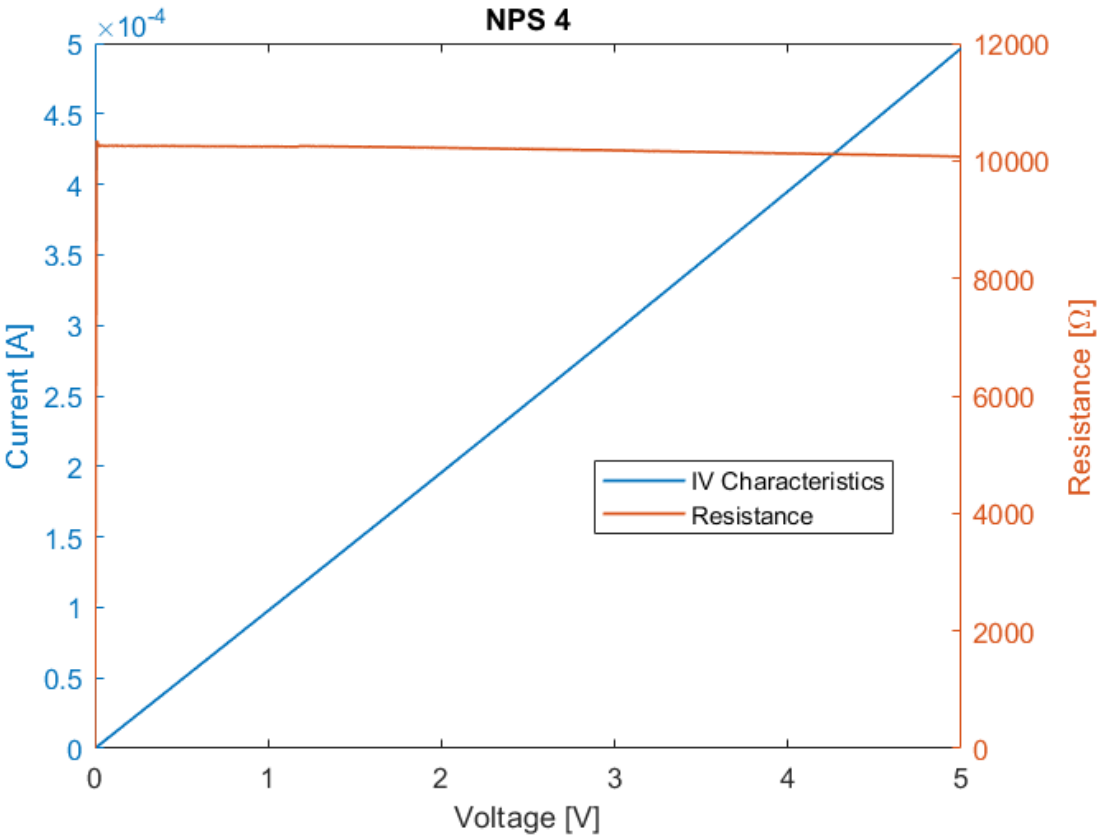

Figure A.6. NPS4 IV characteristics and the dependence of resistance on voltage as measured by a parametric analyzer

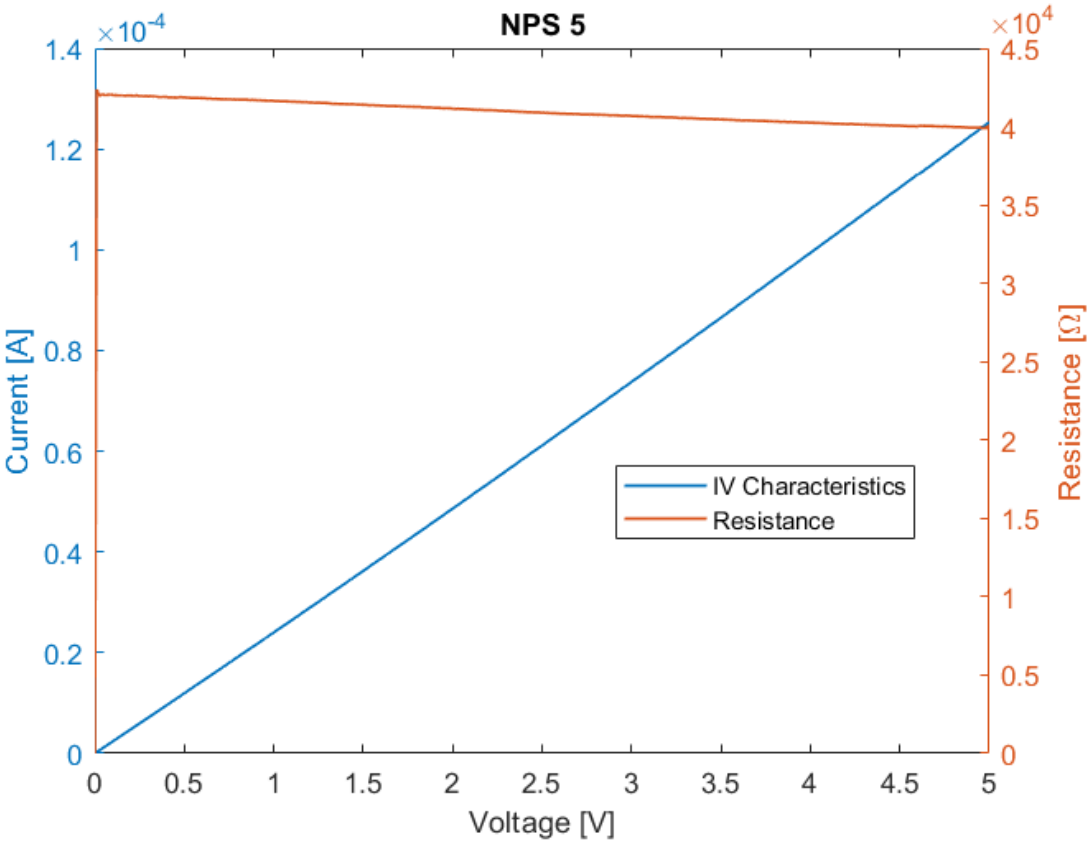

Figure A.7. NPS5 IV characteristics and the dependence of resistance on voltage as measured by a parametric analyzer

List of References

[1] E. Pottmeyer, "The fusion materials irradiation test facility at Hanford," *Journal of Nuclear Materials*, vol. 85-86, no. 1, pp. 463–465, 1979.

[2] J. Hagan, E. Opperman, and A. Trego, "The fusion materials irradiation test (FMIT) facility," *Journal of Nuclear Materials*, vol. 123, pp. 958–964, 1984.

[3] Research and Markets, "Radiation Detection, Monitoring, and Safety Market - Growth, Trends, COVID-19 Impact, and Forecasts(2022 - 2027)" ID 4775049. (2022, June). [Online]. Available: https://www.researchandmarkets.com/reports/4775049/radiation-detection-monitoring-and-safety

[4] K. Persaud and G. Dodd, "Analysis of discrimination mechanisms in the mammalian olfactory system using a model nose," *Nature*, vol. 299, no. 5881, pp. 352–355, Sep. 1982.

[5] A. Wilson and M. Baietto, "Applications and advances in electronic-nose technologies," *Sensors*, vol. 9, no. 7, pp. 5099–5148, 2009 [Online]. Available: https://doi.org/10.3390/s90705099

[6] J. Han, M. Meyyappan, J. Ahn, and Y. Choi, "Liquid gate dielectric field effect transistor for a radiation nose," *Sens. Actuators Phys.*, vol. 182, pp. 1–5, 2012 [Online]. Available: https://doi.org/10.1016/j.sna.2012.05.038

[7] Z. Hameed and J. V. Gats, "Boron-nitride nanotubes and versatile dielectrics for mems electronic nose radiation detection," M.S. thesis, Dept. of Applied Physics, Naval Postgraduate School,, Monterey, CA, USA, 2019.

[8] N. Connor. (2019, Dec.). What is Thermoluminescent Dosimeter - TLD - Definition. [Online]. Available: https://www.radiation-dosimetry.org/what-is-thermoluminescent-dosimeter-tld-definition/

[9] G. F. Knoll, *Radiation Detection and Measurement*, 3rd ed. New York, NY, USA: John Wiley and Sons, 2000.

[10] A. L. Richards. (2013, Jan.). United States Customs and Border Protection's Radiation Portal Monitors and Seaports. Department of Homeland Security Office of Inspector General. [Online]. Available: https://www.oig.dhs.gov/reports/2013-01/united-states-customs-and-border-protections-radiation-portal-monitors-seaports

[11] U. S. Environmental Protection Agency. (2022, July). Radiation and Shipping Port Security. United States Environmental Agency. [Online]. Available: https://www.epa.gov/radtown/radiation-and-shipping-port-security

[12] W. E. Burcham, *Nuclear Physics, An Introduction*, 2nd ed. London, UK: Longman, 1973.

[13] R. Rhodes, *The Making of the Atomic Bomb*. New York, NY: Touchstone, 1988.

[14] JANIS. (2023, Mar.). n-Induced Cross Sections. [Online]. Available: http://www.oecd-nea.org/janisweb/

[15] Y. Sardjono, S. Widodo, Irhas, and H. Tantawy, "A design of boron neutron capture therapy for cancer treatment in Indonesia," *Indonesian Journal of Physics and Nuclear Applications*, vol. 1, no. 1, pp. 1–13, 02 2016 [Online]. Available: https://doi.org/10.24246/ijpna.v1i1.1-13

[16] S. Iijima, "Helical microtubules of graphitic carbon," *Nature*, vol. 354, no. 6348, pp. 56–58, 1991 [Online]. Available: https://doi.org/10.1038/354056a0

[17] M. Monthioux, *Carbon Meta-Nanotubes: Synthesis, Properties and Applications*, Chichester, Ed. Wiley-Blackwell, 2012.

[18] C. Amiot, X. Shuping, L. Song, L. Pan, and J. Zhao, "Near-infrared fluorescent materials for sensing of biological targets," *Sensors*, vol. 8, pp. 3082–3105, May 2008 [Online]. Available: https://doi.org/10.3390s8053082

[19] M. A. White, *Physical Properties of Materials*, 2nd ed. Taylor and Francis Group, LLC, 2012.

[20] P. J. F. Harris, *Carbon Nanotube Science - Synthesis, Properites and Applications*. Cambridge University Press, 2009 [Online]. Available: https://doi.org/10.1002/anie.201000314

[21] N. Saleh, L. Pfefferle, and M. Elimelech, "Aggregation kinetics of multiwalled carbon nanotubes in aquatic systems: measurements and environmental implications," *Environ. Sci. Technol.*, vol. 42, pp. 7963–7969, 2008 [Online]. Available: https://doi.org/10.1021/es801251c

[22] Q. Zaib and F. Ahmad, "Optimization of carbon nanotube dispersions in water using response surface methodology," *ACS Omega*, Jan. 2019 [Online]. Available: https://doi.org/10.1021/acsomega.8b02965

[23] L. Girifalco, M. Hodak, and R. Lee, "Carbon nanotubes, buckyballs, ropes, and a universal graphitic potential," *Phys. Rev. B: Condens. Matter Mater. Phys.*, no. 62, pp. 13 104–13 110, 2000 [Online]. Available: https://doi.org/10.1103/physrevb.62.13104

[24] M. Williams. (2022, June). Boron nitride nanotube fibers get real. Rice University. Rice News. [Online]. [Online]. Available: https://news.rice.edu/news/2022/boron-nitride-nanotube-fibers-get-real

[25] B. Earp *et al.*, "Electrically conductive CNT composites at loadings below theoretical percolation values," *nanomaterials*, vol. 9, no. 491, Mar. 2019 [Online]. Available: https://doi.org/10.3390/nano9040491

[26] D. Abu Saleh, J. Niskanen, Y. Xue, D. Golberg, F. M. Winnik, and A. Sosnik, "Boron nitride nanotube-based amphiphilic hybrid nanomaterials for superior encapsulation of hydrophobic cargos," *Materials Today Chemistry*, vol. 6, pp. 45–50, 2017 [Online]. Available: https://doi.org/https://doi.org/10.1016/j.mtchem.2017.09.003

[27] Arduino Tutorials. (2016, May). Arduino Resistance Measurement. [Online]. Available: https://circuits4you.com/2016/05/13/arduino-resistance-measurement/

[28] H. Vega-Carrillo and C. Torres-Muhech, "Low energy neutrons from a 239pube isotopic neutron source inserted in moderating media," *Revista Mexicana De Fisica - REV MEX FIS*, vol. 48, pp. 405–412, 10 2002.

THIS PAGE INTENTIONALLY LEFT BLANK

Initial Distribution List

1. Defense Technical Information Center
   Ft. Belvoir, Virginia
2. Dudley Knox Library
   Naval Postgraduate School
   Monterey, California